The Astrophysical Journal, 836:132 (21pp), 2017 February 10 https://doi.org/10.3847/1538-4357/aa5b95

The JCMT Gould Belt Survey: A First Look at IC 5146

D. Johnstone[1,2], S. Ciccone[1,3], H. Kirk[1], S. Mairs[1,2], J. Buckle[4,5], D. S. Berry[6], H. Broekhoven-Fiene[1,2], M. J. Currie[6], J. Hatchell[7], T. Jenness[8], J. C. Mottram[9,10], K. Pattle[11], S. Tisi[12], J. Di Francesco[1,2], M. R. Hogerheijde[9], D. Ward-Thompson[11], P. Bastien[13], D. Bresnahan[11], H. Butner[14], M. Chen[1,2], A. Chrysostomou[15], S. Coudé[13], C. J. Davis[16], E. Drabek-Maunder[17], A. Duarte-Cabral[7], M. Fich[12], J. Fiege[18], P. Friberg[6], R. Friesen[19], G. A. Fuller[20], S. Graves[6], J. Greaves[21], J. Gregson[22,23], W. Holland[24,25], G. Joncas[26], J. M. Kirk[11], L. B. G. Knee[1], K. Marsh[27], B. C. Matthews[1,2], G. Moriarty-Schieven[1], C. Mowat[7], D. Nutter[27], J. E. Pineda[20,28,29], C. Salji[4,5], J. Rawlings[30], J. Richer[4,5], D. Robertson[3], E. Rosolowsky[31], D. Rumble[7], S. Sadavoy[10], H. Thomas[6], N. Tothill[32], S. Viti[30], G. J. White[22,23], J. Wouterloot[6], J. Yates[30], and M. Zhu[33]

[1] NRC Herzberg Astronomy and Astrophysics, 5071 West Saanich Road, Victoria, BC, V9E 2E7, Canada
[2] Department of Physics and Astronomy, University of Victoria, Victoria, BC, V8P 1A1, Canada
[3] Department of Physics and Astronomy, McMaster University, Hamilton, ON, L8S 4M1, Canada
[4] Astrophysics Group, Cavendish Laboratory, J J Thomson Avenue, Cambridge, CB3 0HE, UK
[5] Kavli Institute for Cosmology, Institute of Astronomy, University of Cambridge, Madingley Road, Cambridge, CB3 0HA, UK
[6] East Asian Observatory, 660 North A'ohōkū Place, University Park, Hilo, Hawaii 96720, USA
[7] Physics and Astronomy, University of Exeter, Stocker Road, Exeter EX4 4QL, UK
[8] Large Synoptic Survey Telescope Project Office, 933 N. Cherry Avenue, Tucson, Arizona 85721, USA
[9] Leiden Observatory, Leiden University, P.O. Box 9513, 2300 RA Leiden, The Netherlands
[10] Max Planck Institute for Astronomy, Königstuhl 17, D-69117 Heidelberg, Germany
[11] Jeremiah Horrocks Institute, University of Central Lancashire, Preston, Lancashire, PR1 2HE, UK
[12] Department of Physics and Astronomy, University of Waterloo, Waterloo, Ontario, N2L 3G1, Canada
[13] Université de Montréal, Centre de Recherche en Astrophysique du Québec et département de physique, C.P. 6128, succ. centre-ville, Montréal, QC, H3C 3J7, Canada
[14] James Madison University, Harrisonburg, Virginia 22807, USA
[15] School of Physics, Astronomy & Mathematics, University of Hertfordshire, College Lane, Hatfield, Herts, AL10 9AB, UK
[16] Astrophysics Research Institute, Liverpool John Moores University, Egerton Warf, Birkenhead, CH41 1LD, UK
[17] Imperial College London, Blackett Laboratory, Prince Consort Road, London SW7 2BB, UK
[18] Department of Physics & Astronomy, University of Manitoba, Winnipeg, Manitoba, R3T 2N2, Canada
[19] Dunlap Institute for Astronomy & Astrophysics, University of Toronto, 50 St. George Street, Toronto ON M5S 3H4 Canada
[20] Jodrell Bank Centre for Astrophysics, Alan Turing Building, School of Physics and Astronomy, University of Manchester, Oxford Road, Manchester, M13 9PL, UK
[21] Physics & Astronomy, University of St. Andrews, North Haugh, St. Andrews, Fife KY16 9SS, UK
[22] Department of Physical Sciences, The Open University, Milton Keynes MK7 6AA, UK
[23] The Rutherford Appleton Laboratory, Chilton, Didcot, OX11 0NL, UK
[24] UK Astronomy Technology Centre, Royal Observatory, Blackford Hill, Edinburgh EH9 3HJ, UK
[25] Institute for Astronomy, Royal Observatory, University of Edinburgh, Blackford Hill, Edinburgh EH9 3HJ, UK
[26] Centre de recherche en astrophysique du Québec et Département de physique, de génie physique et d'optique, Université Laval, 1045 avenue de la médecine, Québec, G1V 0A6, Canada
[27] School of Physics and Astronomy, Cardiff University, The Parade, Cardiff, CF24 3AA, UK
[28] European Southern Observatory (ESO), Garching, Germany
[29] Max Planck Institute for Extraterrestrial Physics, Giessenbachstrasse 1, D-85748 Garching, Germany
[30] Department of Physics and Astronomy, UCL, Gower Street, London, WC1E 6BT, UK
[31] Department of Physics, University of Alberta, Edmonton, AB T6G 2E1, Canada
[32] University of Western Sydney, Locked Bag 1797, Penrith NSW 2751, Australia
[33] National Astronomical Observatory of China, 20A Datun Road, Chaoyang District, Beijing 100012, China
Received 2016 October 3; revised 2016 December 16; accepted 2017 January 3; published 2017 February 14

Abstract

We present 450 and 850 μm submillimeter continuum observations of the IC 5146 star-forming region taken as part of the James Clerk Maxwell Telescope Gould Belt Survey. We investigate the location of bright submillimeter (clumped) emission with the larger-scale molecular cloud through comparison with extinction maps, and find that these denser structures correlate with higher cloud column density. Ninety-six individual submillimeter clumps are identified using FellWalker, and their physical properties are examined. These clumps are found to be relatively massive, ranging from 0.5 $M_{\odot}$ to 116 $M_{\odot}$ with a mean mass of 8 $M_{\odot}$ and a median mass of 3.7 $M_{\odot}$. A stability analysis for the clumps suggests that the majority are (thermally) Jeans stable, with $M/M_J < 1$. We further compare the locations of known protostars with the observed submillimeter emission, finding that younger protostars, i.e., Class 0 and I sources, are strongly correlated with submillimeter peaks and that the clumps with protostars are among the most Jeans unstable. Finally, we contrast the evolutionary conditions in the two major star-forming regions within IC 5146: the young cluster associated with the Cocoon Nebula and the more distributed star formation associated with the Northern Streamer filaments. The Cocoon Nebula appears to have converted a higher fraction of its mass into dense clumps and protostars, the clumps are more likely to be Jeans unstable, and a larger fraction of these remaining clumps contain embedded protostars. The Northern Streamer, however, has a larger number of clumps in total and a larger fraction of the known protostars are still embedded within these clumps.

Key words: ISM: clouds – ISM: structure – stars: formation – stars: protostars – submillimeter: galaxies – submillimeter: ISM

1. Introduction

The Gould Belt Legacy Survey (GBS; Ward-Thompson et al. 2007) conducted with the James Clerk Maxwell Telescope (JCMT) extensively observed many nearby star-forming regions, tracing the very earliest stages of star formation at 450 and 850 μm with the Submillimetre Common-User Bolometer Array 2 (SCUBA-2; Holland et al. 2006). This imaging covered 50 square degrees of nearby clouds within the Gould Belt, including well-known regions such as Auriga (Broekhoven-Fiene et al. 2016), Ophiuchus (Pattle et al. 2015), Orion (Salji et al. 2015a, 2015b; Kirk et al. 2016a, 2016b; Lane et al. 2016; Mairs et al. 2016), Perseus (Hatchell et al. 2013; Sadavoy et al. 2013; Chen et al. 2016), Serpens MWC 297 (Rumble et al. 2015), Taurus (Buckle et al. 2015; Ward-Thompson et al. 2016), and W40 (Rumble et al. 2016). Among these targets, the GBS survey covered approximately 2.5 square degrees of the IC 5146 star-forming region.

The molecular cloud, IC 5146, is both a reflection nebula and an H II region surrounding the B0 V Star BD+46° 3474 (Herbig & Reipurth 2008, see their Figures 1 and 2). IC 5146 is comprised of two notable features: the first being the Cocoon Nebula, which is a bright core nebula located within a bulbous dark cloud at the end of a long filamentary second feature, the Northern Streamer, extending northwest from the Cocoon Nebula. These two features display distinctly different properties, clustered versus distributed young stars, and therefore present an ideal laboratory for investigating the range of star-formation processes within a single cloud.

In this paper, we take a first look at the submillimeter continuum emission within IC 5146, concentrating on the distribution of dense gas and dust within the cloud and its relation with on-going star formation. In Section 2, we provide background information on IC 5146 and its two main features. The new SCUBA-2 observations along with estimates of the total cloud column density and protostellar content are discussed in Section 3. These observations are analyzed in Section 4, starting from the largest physical scales and zooming in through the submillimeter clumps to the individual young stellar objects (YSOs). Section 5 adds context to the analysis, contrasting star formation in the Cocoon Nebula and the Northern Streamer filaments, and the results are summarized in Section 6.

2. IC 5146

There are varying estimates of the distance to IC 5146. Initially, a distance of 1000 pc was determined by Walker (1959) using photoelectric star observations. A distance of 460 pc was later derived by Lada et al. (1999) using deep near-infrared (HK) imaging observations to compare the number of foreground stars to those expected from galactic models. Herbig & Reipurth (2008) adopt a distance of 1200 ± 180 pc in their review based on the work of Herbig & Dahm (2002) that used spectroscopic distances to late-B stars and two different main-sequence calibrations. An estimation of 1200 pc is quite high in comparison to the Lada estimation but nearer to initial stellar distances measured by Walker (1959) and Elias (1978). For their *Spitzer Space Telescope* analysis of IC 5146, Harvey et al. (2008) re-evaluated the photometric distance using a modern ZAMS calibrator, the Orion Nebula Cluster, and several photometric methods for different members of IC 5146. A distance of 950 ± 80 pc was determined by their analysis and, for consistency with that paper, we use 950 pc throughout the rest of this work.

IC 5146 consists of many distinct populations across two main features, the Cocoon Nebula and the Northern Streamer. Optical and near-infrared identified objects include approximately 20 variable stars, 40 faint stars above the main sequence that are the members of a population of young pre-main-sequence stars, 100 Hα-emission stars (Herbig & Dahm 2002), 110 $M > 1.2\,M_{\odot}$ stars (Forte & Orsatti 1984), and 200 candidate YSOs (Harvey et al. 2008). Using *WISE* data in combination with existing *Spitzer* and Two Micron All Sky Survey (2MASS) observations, Nunes et al. (2016) identify new candidate YSOs in the extended IC 5146 region, including five protostellar clusters (with ~20–50 members each) in the area around the Northern Streamer, as well as a total of ~160 protostars within the cluster at the center of the Cocoon Nebula. The more-evolved stars of the Cocoon Nebula complex are thought to be spatially co-distant with the younger stars still entangled within the current dense gas. Two discrepancies to this claim are the distances determined for BD+46° 3471 and BD+46° 3474 as 355 pc and 400 pc respectively (Harvey et al. 2008). These distances, as well as the Lada et al. (1999) distance of 460 pc, remain problematic because at approximately 400 pc the ages of the K/M-type T Tauri stars in the cluster jump from 0.2 to 15 Myr (Harvey et al. 2008). The later isochronal age is inconsistent with the fact that IC 5146 has a high number of accreting pre-main-sequence stars, as well as the appearance of nebulosity observed in the region. Indeed, this evidence of on-going star formation argues for an age of less than a few megayears for the region. There is also strong circumstantial evidence that the two main components of IC 5146, the Cocoon Nebula and the Northern Streamer, are co-distant. First, the Cocoon Nebula appears to be connected to a long filament with the Northern Streamer forming at the opposite end. Second, the molecular gas associated with the Cocoon Nebula has velocities consistent with those seen in the rest of the IC 5146 region (Dobashi et al. 1993).

The total H_2 molecular mass of the central IC 5146 cloud complex has been estimated to be approximately 4000 $M_{\odot}$, similar to that of the Taurus complex, as measured by Dobashi et al. (1992, 1993) using ^{12}CO ($J = 1 - 0$), ^{13}CO ($J = 1 - 0$), and C^{18}O ($J = 1 - 0$) emission lines. The total mass estimates of H I and H II, respectively, are approximately 670 $M_{\odot}$ and 4.5 $M_{\odot}$ as determined by Samson (1975) or 445 ± 105 $M_{\odot}$ and 9.8 ± 1 $M_{\odot}$ as determined by Roger & Irwin (1982). All of these mass estimates were made assuming a distance to the cloud of approximately 1 kpc. The median age for the cluster, based on isochrone fits to the optical and near-infrared pre-main-sequence stars, is approximately 1.0 Myr (Herbig & Dahm 2002; Herbig & Reipurth 2008), in rough agreement with the young ages determined for the K/M-type T Tauri stars.

2.1. The Cocoon Nebula

The molecular cloud structure southeast of the Northern Streamer is noticeably bright and active due in part to the presence of BD+46° 3474 and the high-luminosity variable star V1735 Cyg from which X-ray emission has been detected (Skinner et al. 2009).

The Cocoon is a more-evolved H II star-forming region relative to younger complexes found in the Orion or Ophiuchus

Table 1
Noise Values within the SCUBA-2 Maps

Region	Name[a]	R.A.[b] (J2000.0)	Decl.[b] (J2000.0)	σ_{850}[c] (mJy arcsec^{-2})	σ_{450}[c]	σ_{850}[d] (mJy bm^{-1})	σ_{450}[d]
Coccon Nebula	IC5146-H2	21:53:45	47:15:22	0.050	1.4	3.7	67
Northern Streamer	IC5146-E	21:48:31	47:31:48	0.045	1.1	3.3	53
Northern Streamer	IC5146-W	21:45:36	47:36:59	0.049	1.4	3.6	67

Notes.
[a] Observation designation chosen by the GBS team, denoted as Target Name in the CADC database at http://www3.cadc-ccda.hia-iha.nrc-cnrc.gc.ca/en/jcmt/. The Proposal ID for all these observations is MJLSG36.
[b] Central position of each observation.
[c] Pixel-to-pixel (rms) noise within each region after mosaicking together all observations.
[d] Effective noise per beam (i.e., point source sensitivity) within each region after mosaicking together all observations.

clouds, showing decreased small-scale structure due to density inhomogeneities expanding into more diffuse surroundings (Israel 1977; Wilking et al. 1984). The dust has dispersed into a mottled structure, as evidenced from scattered light, suggesting that the collective activity of the stars in this region has blown out material from the center. There is further evidence of dispersal due to the presence of BD+46° 3474 itself, which is the most massive star in IC 5146 and is responsible for the observed gas and dust emission surrounding the H II region (Wilking et al. 1984). Cluster stars appear to have formed in a dense foreground section of the molecular cloud. BD+46° 3474, however, has evacuated a blister cavity out of which gas and dust are now flowing through a funnel-shaped volume and dissipating the cloud region (Herbig & Dahm 2002).

More than 200 YSO candidates have been identified throughout IC 5146 using observations from the *Spitzer Space Telescope*, and the population near the Cocoon Nebula is more evolved, based on spectral observations, when compared to the younger YSOs found in the Northern Streamer (Harvey et al. 2008). High-velocity CO outflows were identified around many protostellar candidates, based on the IRAS Point Source Catalog (Dobashi et al. 1993, 2001). Thus, this region of the molecular cloud remains active, exhibiting an extended period of development.

2.2. The Northern Streamer

The Northern Streamer is comprised of a network of near-parallel filaments in which star formation is occurring. Twenty-seven filaments were identified using *Herschel* continuum data and traced throughout the region (Arzoumanian et al. 2011). The observed substructure within these filaments suggests that they are the primary birth sites of prestellar cores (Di Francesco 2012; Polychroni et al. 2013). We identify both cores and YSOs along the filamentary sections of the streamer (see Sections 4.2 and 4.3), supporting the notion that here large-scale filament morphology plays a role in the production of stars.

In this paper, we do not characterize or identify any singular filamentary structures by a modeling algorithm, but we do study and analyze the general morphology of the filamentary and clump structures seen in the streamer. Recently, Pon et al. (2011, 2012) showed that filamentary geometry at this scale is the most favorable scenario in which isothermal perturbations grow before global collapse overwhelms the region dynamics, with the filamentary ends most likely to collapse first. In some numerical simulations, nearly all cores that are detected are associated with filaments and most of these eventually form protostars (e.g., Mairs et al. 2014). Observations also suggest a strong connection between filaments and cores: various *Herschel* analyses have found that between two-thirds and three-quarters of cores are located along filaments (Polychroni et al. 2013; Schisano et al. 2014; Könyves et al. 2015). Collapse patterns in the Cocoon Nebula and Northern Streamer provide an opportunity to strengthen our understanding about the processes playing a pivotal role in fragmenting molecular clouds.

3. Observations and Data Reduction

3.1. SCUBA-2

IC 5146 was observed with SCUBA-2 (Holland et al. 2013) at 450 and 850 μm simultaneously as part of the JCMT Gould Belt Survey (GBS, Ward-Thompson et al. 2007). The SCUBA-2 observations were obtained between 2012 July 8 and 2013 July 14. These data were observed as three fully sampled 30′ diameter circular regions using the PONG 1800 mode (Kackley et al. 2010). Each area of the sky was observed six times. Neighboring fields were set up to overlap slightly to create a more uniform noise in the final mosaic. Details for these observations are provided in Table 1, and the full IC 5146 region, observed at 850 μm, is shown in Figure 1. Figures 2 and 3 focus on the areas of 450 and 850 μm emission within Cocoon Nebula and the Northern Streamer, respectively.

The data reduction used for the maps presented here follows the GBS Legacy Release 1 methodology (GBS LR1) using the JCMT's Starlink software (Currie et al. 2014),[34] which is discussed by Mairs et al. (2015). The data presented here were reduced using an iterative map-making technique (makemap in SMURF),[35] and gridded to 2″ pixels at 450 μm and 3″ pixels at 850 μm. The iterations were halted when the map pixels, on average, changed by <0.1% of the estimated map rms. These initial automask reductions of each individual scan were co-added to form a mosaic from which a signal-to-noise ratio (S/N) mask was produced for each region. The final external mask mosaic was produced from a second reduction using this S/N mask to define areas of emission. In IC 5146, the S/N mask included all pixels with S/Ns of 2 or higher at 850 μm. Testing by our data reduction team showed similar final maps using either an 850 μm-based or a 450 μm-based mask for the 450 μm reduction, when using the S/N-based masking scheme described

[34] Available at http://starlink.eao.hawaii.edu/starlink.
[35] SMURF is a software package used for reducing JCMT observations, and is described in more detail by Jenness et al. (2013) and Chapin et al. (2013a, 2013b).

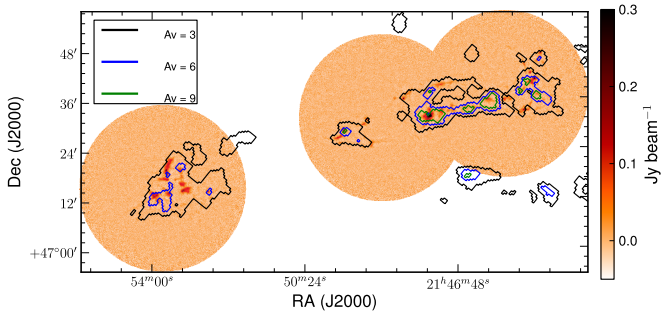

Figure 1. IC 5146 observed at 850 μm with SCUBA-2. Also shown are the $A_V = 3$, 6, and 9 contours from the 2MASS-based extinction map (Section 3.2). The *Spitzer* coverage of the region (Section 3.3) is almost identical to the SCUBA-2 coverage shown here.

here. Using identical masks at both wavelengths for the reduction ensures that the same large-scale filtering is applied to the observations at both wavelengths (e.g., maps of the ratio of flux densities at both wavelengths are less susceptible to differing large-scale flux recovery). Detection of emission structure and calibration accuracy are robust within the masked regions, but are less certain outside of the mask (Mairs et al. 2015).

Larger-scale structures are the most poorly recovered outside of the masked areas, while point sources are better recovered. A spatial filter of 600″ is used during both the automask and external mask reductions, and an additional filter of 200″ is applied during the final iteration of both reductions to the areas outside of the mask. Further testing by our data reduction team found that for 600″ filtering, flux recovery is robust for sources with a Gaussian FWHM of less than 2.′5, provided the mask is sufficiently large. Sources between 2.′5 and 7.′5 in diameter were detected, but both the flux density and the size were underestimated because Fourier components representing scales greater than 5′ were removed by the filtering process. Detection of sources larger than 7.′5 is dependent on the mask used for reduction.

The data are calibrated in mJy per square arcsecond using aperture flux conversion factors of 2.34 Jy/pW/arcsec^2 ± 0.08 Jy/pw/arcsec^2 and 4.71 Jy/pW/arcsec^2 ± 0.5 Jy/pw/arcsec^2 at 850 μm and 450 μm, respectively, as derived from average values of JCMT calibrators (Dempsey et al. 2013). The PONG scan pattern leads to lower noise in the map center and mosaic overlap regions, while data reduction and emission artifacts can lead to small variations in the noise over the whole map. The pointing accuracy of the JCMT is smaller than the pixel sizes we adopt, with current rms pointing errors of 1.″2 in azimuth and 1.″6 in elevation (see http://www.eaobservatory.org/JCMT/telescope/pointing/pointing.html); JCMT pointing accuracy in the era of SCUBA is discussed by Di Francesco et al. (2008).

The observations for IC 5146 were taken in grade 2 ($0.05 < \tau_{225\,\mathrm{GHz}} < 0.08$) weather, corresponding to $0.21 < \tau_{850\,\mu\mathrm{m}} < 0.34$ (Dempsey et al. 2013), with a mean value plus standard deviation of $\tau_{225\,\mathrm{GHz}}$ of 0.063 ± 0.006. At 850 μm, the final noise level in the mosaic is 0.048 mJy arcsec^{-2} per 3″ pixel, corresponding to a point source sensitivity of 3.7 mJy per 14.″6 beam. At 450 μm, the final noise level is 1.3 mJy arcsec^{-2} per 2″ pixel, corresponding to a point source sensitivity of 62 mJy per 9.″8 beam (see Table 1 for details by individual region). The beam sizes quoted here are the effective beams determined by Dempsey et al. (2013), and account for the fact that the beam shape is well-represented by the sum of a Gaussian primary beam shape and a fainter, larger Gaussian secondary beam.

The SCUBA-2 450 and 850 μm observations were convolved to a common beam size and compared to estimate the temperature of the emitting dust (see Appendix A). A clump temperature of 15 K is adopted throughout the remainder of this paper based on these results. Given that the CO ($J = 3 - 2$) rotational line lies in the middle of the 850 μm bandpass (Johnstone et al. 2003; Drabek et al. 2012), an analysis was undertaken to determine the level of CO contamination for those limited areas of the map where CO observations also exist (see Appendix B). The contamination results show that none of the bright 850 μm emission is contaminated by more than 10%. Thus, for the remainder of this paper we use the uncorrected 850 μm map to determine source properties. All of the data presented in this paper are publicly available at https://doi.org/10.11570/17.0001.

Kramer et al. (2003) previously imaged parts of IC 5146 at the JCMT with SCUBA (Holland et al. 1999) at both 450 and 850 μm, reducing the data using the SCUBA User Reduction Facility (SURF; Jenness et al. 2002) and correcting for atmospheric extinction and sky noise. The SCUBA mapped region is ∼14′ × 2.′5 in size and includes parts of the Northern Streamer, focusing on ridges. The authors find several peaks of high emission (corresponding to optical extinctions of >20 mag) in their maps that they attribute to dense prestellar structures and identify four clumps with high optical extinctions along ridges in the region. They construct a dust temperature map and conclude that there is a distribution of temperatures throughout the region, varying between 10 and 20 K, with an average of 16.5 ± 8 K, in agreement with the values determined in Appendix A. The temperatures of the cores tend toward the lower limit, $T_c \sim 12$ K. Assuming this temperature and a dust emissivity of $\kappa_{850} = 0.01$ cm^2 g^{-1}, their derived core masses vary between 4 $M_\odot$ and 7 $M_\odot$ at their adopted distance of 460 pc (these masses increase by about a factor of four at our adopted distance of 950 pc). The resolution of their maps was smoothed beyond the native JCMT resolution and so finer detail in the cloud structure was not analyzed. These original reductions are not directly available for comparison. The SCUBA Legacy Catalog reduction (Di Francesco et al. 2008) of the Northern Streamer, however, is available in the archive and was used to verify that the SCUBA-2 GBS data sets presented here are in broad agreement with the lower sensitivity Kramer et al. (2003) observations.

3.2. Extinction Map

Cambrésy (1999) first published an extinction map of the IC 5146 region using optical R-band star counts based on the comparison of local stellar densities (L. Cambrésy 1999). A more recent version of this IC 5146 extinction map (L. Cambrésy 2015, private communication) was derived using 2MASS near-infrared H-K data to measure stellar reddening that was then used to estimate the local extinction in the region following the technique described by Cambrésy et al. (2002). The spatial resolution of this unpublished map is 2′. Notably, known YSOs and foreground stars have not been removed during the map construction. Nevertheless, the quality and

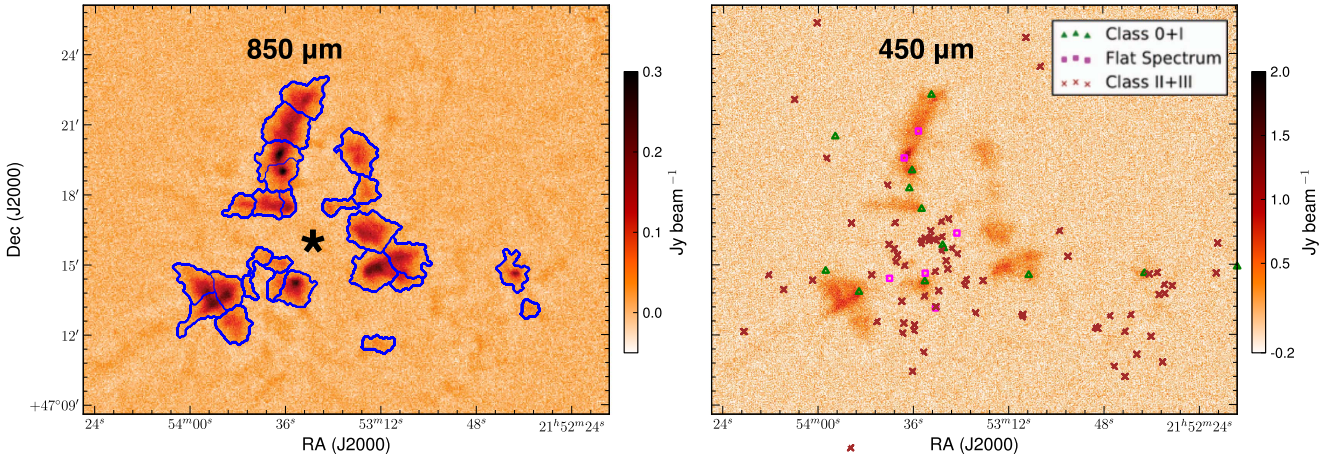

Figure 2. IC 5146 Cocoon Nebula. The left panel shows 850 μm dust continuum emission. The right panel shows 450 μm dust emission. Overlaid on the 850 μm map are contours denoting the boundaries of the clumps identified in this paper (Section 4.2), while on the 450 μm map the locations of the *Spitzer*-classified YSOs, by type (see the legend), are provided (Section 4.3). In this region, there are 13 Class 0/I, 6 Flat, 65 Class II, and 9 Class III YSOs. The black star in the left panel shows the location of the B0 V Star BD+46° 3474 (Herbig & Reipurth 2008).

resolution of this extinction map remain sufficent for the analysis required here. Figure 1 shows the $A_V = 3$, 6, and 9 contours from the extinction map overlaid on the dust continuum SCUBA-2 850 μm map.

3.3. Spitzer YSOs

The *Spitzer Space Telescope* observed the IC 5146 region (Harvey et al. 2008) using its InfraRed Array Camera (IRAC) and its Multiband Imaging Photometer for *Spitzer* (MIPS). The region observed by *Spitzer* is almost identical to the SCUBA-2 areal coverage shown in Figure 1. Over 200 candidate YSOs were identified in the region. Those sources with both IRAC and MIPS detections have been independently classified as Class 0+1, Flat, Class II, and Class III protostars by Dunham et al. (2015) as part of a larger analysis of YSOs throughout the entire Gould Belt. Dunham et al. (2015) determine YSO class through careful examination of the IR spectral energy distributions (SEDs) and their final catalog contains an analysis of contamination by background AGB stars, updated extinction corrections, and revised SEDs, improving upon previous *Spitzer* YSO catalogs by Harvey et al. (2008) and Evans et al. (2009).

The *Spitzer* survey results combined with the GBS SCUBA-2 continuum data sets are shown in Figures 2 and 3. There are 131 *Spitzer* sources within the boundaries of the SCUBA-2 observations. Notably, the youngest YSOs, i.e., Class 0/I and Flat sources, are positioned near areas of dust emission, with few outliers whereas the older, Class II and III sources are more scattered.

4. Analysis

Near-infrared extinction maps (e.g., Cambrésy 1999) typically trace the large-scale structure in a cloud complex while SCUBA-2 maps focus on denser, localized dust emission (e.g., Ward-Thompson et al. 2016) and the identification of sources from the *Spitzer* survey traces the specific locations of YSOs (Dunham et al. 2015). Considered together, these three diverse data sets help us to build a better model of how star formation is influenced at each scale.

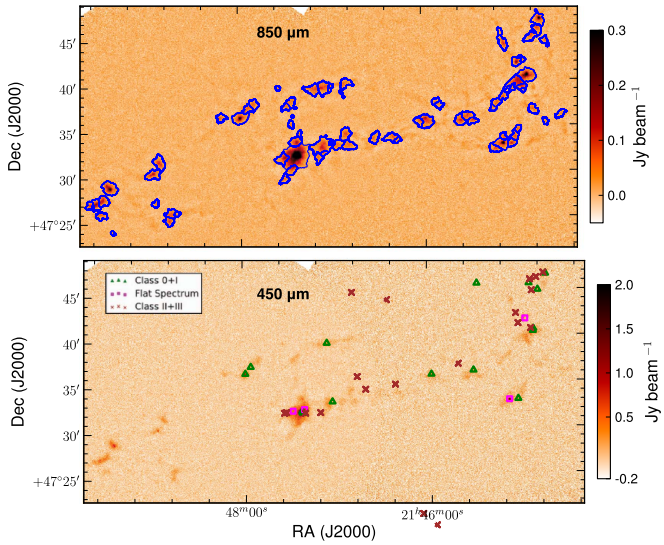

Figure 3. IC 5146 Northern Streamer. Upper panel shows 850 μm dust continuum emission. Lower panel shows 450 μm dust emission. Overlaid on the 850 μm map are contours denoting the boundaries of the clumps identified in this paper (Section 4.2) while on the 450 μm map the locations of the YSOs, by type (see legend), are provided (Section 4.3). In this region there are 15 Class 0/I, 4 Flat, 14 Class II, and 6 Class III YSOs.

4.1. Large-scale Structure

To investigate the connection between emission in the 850 μm SCUBA-2 map and the observed extinction, we restrict our continuum analysis to 850 μm pixels above an S/N of 3.5, which results in a cut of pixels below a value of 0.175 mJy arcsec^{-2}. This threshold is chosen to prevent the total flux density measured being dominated by the noise from the large number of pixels with little signal. The extinction map, as introduced and discussed in Section 3.2, has a small number of zones with negative extinction caused by artifacts in the data set. We exclude these pixels from our extinction map analysis; noting that they make up only 6% of the total map area analyzed.

Under the assumption that the optical characteristics of the dust grains remain the same throughout IC 5146 and that the

temperature of the dust is constant, the mass revealed by the 850 μm map is directly proportional to the integrated flux density. Following Hildebrand (1983), the submillimeter-derived mass, M_{850} is

$$M_{850} = \frac{S_{850}\, d^2}{\kappa_{850}\, B_{850}(T_d)}, \quad (1)$$

where d is the distance to the cloud, S_{850}, κ_{850}, and B_{850} are the integrated flux density, opacity, and Planck function measured at 850 μm respectively, and T_d is the dust temperature. The opacity of the dust is quite uncertain and a source of significant on-going research. Following the GBS standard (Pattle et al. 2015; Rumble et al. 2015, 2016; Salji et al. 2015a, 2015b; Kirk et al. 2016a, 2016b; Lane et al. 2016; Mairs et al. 2016), we adopt $\kappa_{850} = 0.0125\,\mathrm{cm^2\,g^{-1}}$. Taking a fiducial value for the temperature from Appendix A, $T_d = 15$ K (consistent with that used by Kramer et al. 2003), and assuming a distance to IC 5146, $d = 950$ pc (Harvey et al. 2008), Equation (1) becomes

$$M_{850} = 11.3 \left(\frac{S_{850}}{\mathrm{Jy}}\right)\left(\frac{d}{950\ \mathrm{pc}}\right)^2 \times \left(\frac{\kappa_{850}}{0.0125\ \mathrm{cm^2\ g^{-1}}}\right)^{-1} \left[\frac{\exp\left(\frac{17\ \mathrm{K}}{T_d}\right) - 1}{\exp\left(\frac{17\ \mathrm{K}}{15\ \mathrm{K}}\right) - 1}\right] M_\odot. \quad (2)$$

Note that decreasing the fiducial dust temperature to 10 K would raise the derived masses by about a factor of two.

The extinction map can also be used to derive masses assuming a linear relation between extinction and column density. We adopt the Savage & Mathis (1979) ratio of $N_H/A_V = 1.87 \times 10^{21}$ cm^{-2} mag^{-1} and assume a mean molecular weight $\mu = 2.37$ (Kauffmann et al. 2008).

In Figure 4, we show the cumulative fraction of mass within IC 5146 as a function of minimum extinction cut-off. The orange curve plots the mass derived from the extinction map using only the footprint of the SCUBA-2 observations. This curve reveals that most of the mass within the cloud lies at low extinction, with 50% of the mass below an extinction of $A_V = 3$. Alternatively, the blue curve plots the mass derived from the SCUBA-2 850 μm map (Equation (2)), assuming that the flux density is a direct linear proxy for column density. The cumulative curve clearly shows that the SCUBA-2 flux predominantly traces the higher extinction regions within the cloud, with 85% of the mass derived from the submillimeter continuum residing at an extinction greater than $A_V = 3$ and 50% of the mass at an extinction greater than $A_V = 6$. This result is similar to those found for other star-forming regions (e.g., Onishi et al. 1998; Johnstone et al. 2004; Hatchell et al. 2005; Enoch et al. 2006, 2007; Kirk et al. 2006; Könyves et al. 2013). Namely, the compact submillimeter emission within IC 5146 is intrinsically linked and heavily biased to regions of high dust column.

In total, we obtain a submillimeter-derived mass of $\sim$670 $M_\odot$ for the IC 5146 region, above the S/N = 3.5 cut-off. Taking only the extinction-derived mass coincident with the SCUBA-2 coverage, we obtain a mass of 16,000 $M_\odot$ and a mean extinction of $A_V = 1.7$. This latter mass is about four times the CO mass estimate derived by Dobashi et al. (1992, 1993). The discrepancy between the CO-derived mass and the extinction-derived mass suggests one or both of the following situations: that a fraction of the extinction toward IC 5146 is unassociated with the cloud itself, and thus the extinction mass is somewhat over-estimated, or that the CO observations were not sensitive to the extended low A_V emission from IC 5146, which is suggested by the comparison of the ^{12}CO and ^{13}CO images presented by Dobashi et al. (1992). The extinction mass corresponds to roughly 24 times the submillimeter-derived mass. At $A_V > 10$, we find 120 $M_\odot$ in the submillimeter map and $\sim$740 $M_\odot$ in the extinction map. Breaking down the mass estimates by sub-region within IC 5146, we find that the extinction-derived mass coincident with the single SCUBA-2 map covering the Cocoon Nebula is 5100 $M_\odot$, or about one-third of the entire mass for the IC 5146 region. The submillimeter-derived mass for this same region is 285 $M_\odot$, or just over 40% of the dense gas and dust in all of IC 5146. For the Northern Streamer, the extinction-derived mass coincident with the two SCUBA-2 PONGs is $\sim 10^4$ $M_\odot$, whereas the submillimeter-derived mass is 385 $M_\odot$. Table 2 presents a breakdown of the extinction-derived mass, submillimeter-derived mass, and YSO count as a function of A_V threshold and sub-region.

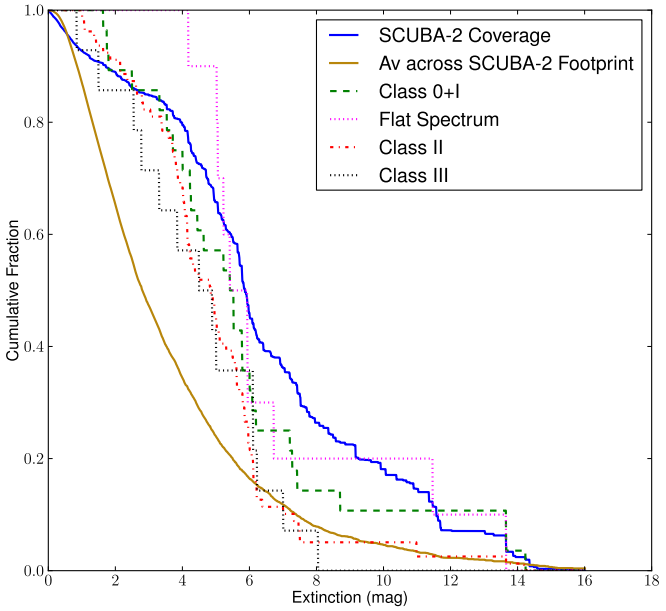

Figure 4. Cumulative mass as a function of extinction. The orange line plots the extinction-derived mass from the Cambrésy extinction map restricted to the SCUBA-2 areal coverage. The blue line plots the distribution of the submillimeter-derived mass from the 850 μm SCUBA-2 map, as a function of the coincident Cambrésy extinction. The colored dash lines show the cumulative distributions of the YSOs, by Class, as a function of the coincident Cambrésy extinction.

4.2. Submillimeter Clumps

We used the FellWalker algorithm (Berry 2015), part of the CUPID package (Berry et al. 2007, 2013) in Starlink, to identify notable structures in the 850 μm dust continuum map from SCUBA-2. The FellWalker technique searches for sets of disjoint clumps, each containing a single significant peak, using a gradient-tracing scheme. The algorithm is qualitatively similar to the better known Clumpfind (Williams et al. 1994) method that has been used extensively. The Fellwalker method,

Table 2
Cumulative Mass above Different Extinction Thresholds

Extinction (mag)	Cloud Area (%)	M_{ext} ($M_\odot$)	M_{ext} (%)	M_{s2} ($M_\odot$)	M_{s2} (%)	M_{s2}/M_{ext} (%)	C0+I+F (%)	CII (%)	CIII (%)
S2 Coverage: 0	100	16051	100	670.3	100	4	100	100	100
2	30	10472	65	596.5	89	6	92	91	86
5	6	3844	24	440.7	66	11	66	46	43
10	1	742	5	121.4	18	16	13	5	0
Cocoon Neb.: 0	100	5125	100	285.4	100	6	100	100	100
2	32	3479	68	88.7	31	3	100	91	89
5	5	976	19	29.4	10	3	79	46	44
10	0	0	0	0.0	0	⋯	0	0	0
N. Streamer: 0	100	10926	100	384.9	100	4	100	100	100
2	28	6993	64	335.5	87	5	84	93	80
5	6	2868	26	240.0	62	8	53	43	40
10	1	742	7	121.4	32	16	26	29	0

however, is more stable against noise and less susceptible to small changes in the input parameters (Watson 2010).

We ran FellWalker with several parameters changed from the default recommended values to achieve two goals: to recover faint but visually distinct objects missed with the default settings and to subdivide several larger structures that had visually apparent substructure not captured with the default settings. Table 3 lists the non-default parameters we adopted. Note that FellWalker assumes a single global noise value for its calculations, while our observations have some variation in noise level: the center of each PONG is about 20% less noisy than the typical rms, and in the Streamer, the overlap area between the two neighboring PONGS is about 25% less noisy, while the edges of the mosaic have a higher noise level than the typical rms. This observational fact informs our two-part clump-identification strategy: we first identify candidate clumps using FellWalker criteria that are generally more relaxed than the default values, and then run an independent program to cull this candidate clump list to ensure that all sources satisfy the same local S/N criteria. To achieve our first goal of recovering faint but visually distinct objects, we lowered the minimum flux density value allowed in clump pixels below the default value (see the "Noise" parameter in Table 3). Allowing fainter pixels to be associated with clumps also led to the identification of some spurious noise features as clumps. We eliminated these false positive clumps through the use of an automated procedure wherein each clump was required to have 10 or more pixels with a local S/N value of 3.5 or higher. (Note that clumps passing this test are allowed to contain additional pixels with lower local S/N values.) This automated procedure reduced the initial FellWalker catalog from 273 clump candidates to 96 reliable clumps. All of these 96 reliable clumps also passed a visual inspection. We note that the vast majority of these clumps also have a good correspondence to the clump catalog obtained using the default FellWalker settings. Namely, about 10% of the clumps in our catalog were either subdivided less or were not identified using the default settings.

Table 4 reports the observed properties of the 96 reliable clumps, including the peak flux densities F_{850} and F_{450} in Jy bm^{-1}, the total integrated flux density at 850 μm within the clump boundary S_{850} in Jy, and the areal extent of each clump A in arcsec^2. As noted in Section 3.1, the SCUBA-2 850 μm bandpass straddles the CO($J = 3 - 2$) rotational line that can result in CO contamination of the continuum flux. Where possible, the peak and total flux density at 850 μm associated with each clump have been investigated for possible CO contamination (Appendix B) and in all cases the contamination values are found to be less than 10%. The results shown are not corrected for CO contamination.

Table 3
FellWalker Parameters

Name	Descriptor	Value
AllowEdge	exclude clumps touching the noisier map edge	0.00
CleanIter	smooth clump edges	15.0
rms	as measured in the map	0.05
FlatSlope	increase the gradient required for associating pixels with a peak	2.0*rms
MinDip	reduce the difference between peaks required to have multiple objects	1.5*rms
MaxJump	reduce the search radius to combine peaks into a single object	2.0
MinPix	minimum number of pixels per clump	10.0
Noise	allow fainter pixels to be associated with a peak	0.35*rms

Table 5 presents the derived properties of the clumps. The effective radius of each clump, R_C in pc, is derived through equating the area within the clump boundary with that of a circular aperture. The masses of the clumps are computed using Equation (2) under the assumption that $T_d = 15$ K (Section 3.1 and Appendix A). Decreasing the dust temperature to 10 K raises the derived masses by about a factor of two. The masses span a range from 0.5 $M_\odot$ to 116 $M_\odot$, the mean clump mass is 8 $M_\odot$, and the median clump mass is 3.7 $M_\odot$. The total mass in clumps is $\sim$750 $M_\odot$, slightly larger than the submillimeter-derived mass found in the previous section. This difference is because we allow the clump boundaries to include not only the bright central emission, but also extended more diffuse emission (below a local S/N = 3.5 level) that is clearly associated. In our analysis in Section 4.1, we use a conservative global S/N = 3.5 threshold to prevent noise spikes at lower S/N levels from being included in our results. Since most of the area of our map appears to lack real emission, noise spikes would make a significant contribution to flux measured at levels below an S/N of 3.5.

Table 4
Identified 850 μm Clumps

Clump[a] Number	Source Name[b] (MJLSG...)	R.A.[c] (J2000.0)	Decl.[c] (J2000.0)	Peak Flux[d] F_{850} (Jy/Bm)	Peak Flux[d] F_{450} (Jy/Bm)	Total Flux[d] S_{850} (Jy)	Area[d] A (arcsec^2)
1	J214428.6+473616	21:44:28.57	47:36:15.80	0.05	0.46	0.16	2457
2	J214439.4+474416	21:44:39.35	47:44:16.02	0.07	0.47	0.14	2151
3	J214439.4+473522	21:44:39.40	47:35:22.03	0.05	0.48	0.09	1305
4	J214442.8+474641	21:44:42.80	47:46:41.03	0.36	1.54	0.92	5292
5	J214443.6+474532	21:44:43.59	47:45:32.27	0.08	0.52	0.32	3051
6	J214448.1+474458	21:44:48.15	47:44:57.60	0.09	0.49	0.31	3573
7	J214448.9+473649	21:44:48.93	47:36:48.82	0.07	0.46	0.27	3168
8	J214452.2+474032	21:44:52.16	47:40:31.76	0.41	1.62	2.10	8163
9	J214454.3+474214	21:44:54.25	47:42:14.36	0.06	0.40	0.08	990
10	J214454.8+473903	21:44:54.79	47:39:02.51	0.08	0.45	0.07	693
11	J214455.6+473927	21:44:55.61	47:39:26.75	0.16	0.65	0.42	1836
12	J214458.2+474154	21:44:58.17	47:41:54.48	0.19	0.67	0.56	3258
13	J214458.2+474003	21:44:58.18	47:40:03.48	0.16	0.69	1.44	5832
14	J214458.8+473434	21:44:58.80	47:34:33.65	0.08	0.51	0.16	1566
15	J214459.7+473937	21:44:59.74	47:39:36.92	0.10	0.52	0.15	1332
16	J214460.7+473355	21:44:60.68	47:33:55.18	0.08	0.69	0.29	2340
17	J214462.9+473302	21:44:62.90	47:33:01.81	0.12	0.64	0.37	2574
18	J214506.5+474357	21:45:06.45	47:43:56.82	0.10	0.49	0.51	5184
19	J214507.5+473345	21:45:07.53	47:33:45.11	0.08	0.54	0.20	1719
20	J214507.7+473809	21:45:07.70	47:38:09.17	0.08	0.52	0.24	2493
21	J214508.2+473306	21:45:08.22	47:33:06.31	0.43	2.01	1.25	5562
22	J214512.9+473723	21:45:12.87	47:37:22.60	0.07	0.50	0.27	2601
23	J214513.3+473235	21:45:13.34	47:32:34.73	0.09	0.55	0.34	3033
24	J214514.1+473705	21:45:14.10	47:37:04.95	0.07	0.46	0.10	1368
25	J214527.7+473545	21:45:27.66	47:35:44.64	0.11	0.50	0.28	2241
26	J214531.1+473616	21:45:31.14	47:36:15.57	0.10	0.61	0.52	3636
27	J214535.4+473541	21:45:35.38	47:35:40.70	0.11	0.67	0.60	3789
28	J214550.8+473736	21:45:50.81	47:37:35.72	0.06	0.43	0.16	2061
29	J214552.3+473745	21:45:52.27	47:37:45.10	0.07	0.45	0.11	1512
30	J214558.8+473602	21:45:58.75	47:36:01.74	0.17	0.74	0.98	5940
31	J214561.5+473550	21:45:61.45	47:35:50.42	0.12	0.45	0.32	2511
32	J214617.8+473345	21:46:17.75	47:33:45.43	0.07	0.53	0.12	1305
33	J214620.4+473407	21:46:20.37	47:34:07.06	0.08	0.61	0.34	3771
34	J214632.8+473355	21:46:32.84	47:33:55.02	0.06	0.65	0.26	3591
35	J214649.8+473314	21:46:49.82	47:33:13.90	0.07	0.46	0.38	4311
36	J214650.0+473429	21:46:49.96	47:34:28.93	0.08	0.41	0.45	4536
37	J214651.3+473953	21:46:51.33	47:39:53.24	0.07	0.44	0.33	4500
38	J214656.9+473312	21:46:56.94	47:33:12.48	0.06	0.38	0.28	3438
39	J214660.2+473949	21:46:60.24	47:39:49.21	0.07	0.33	0.11	1206
40	J214704.4+473241	21:47:04.41	47:32:41.12	0.10	0.45	0.18	1125
41	J214706.2+473936	21:47:06.21	47:39:35.50	0.12	0.45	0.77	5472
42	J214706.4+473306	21:47:06.43	47:33:05.55	0.14	0.51	1.35	10863
43	J214708.9+473157	21:47:08.95	47:31:57.09	0.06	0.37	0.24	2592
44	J214709.2+473933	21:47:09.19	47:39:33.14	0.09	0.44	0.62	5139
45	J214720.5+473433	21:47:20.48	47:34:32.52	0.05	0.39	0.09	1152
46	J214722.7+473342	21:47:22.66	47:33:41.97	0.16	0.60	0.78	3996
47	J214722.8+473212	21:47:22.84	47:32:12.01	0.70	2.92	10.34	21312
48	J214724.8+473103	21:47:24.75	47:31:03.40	0.19	0.63	0.72	3204
49	J214724.8+473815	21:47:24.78	47:38:15.41	0.07	0.40	0.26	3105
50	J214726.6+473534	21:47:26.58	47:35:33.78	0.06	0.31	0.12	1566
51	J214729.0+473734	21:47:29.01	47:37:34.28	0.06	0.39	0.18	2304
52	J214730.3+473202	21:47:30.26	47:32:01.53	0.19	0.67	0.92	4275
53	J214730.6+472935	21:47:30.55	47:29:34.59	0.07	0.38	0.21	2556
54	J214733.5+473944	21:47:33.51	47:39:44.18	0.05	0.42	0.05	837
55	J214750.6+473751	21:47:50.64	47:37:50.54	0.08	0.44	0.28	3024
56	J214753.9+473736	21:47:53.93	47:37:36.16	0.07	0.50	0.33	2880
57	J214759.1+473625	21:47:59.11	47:36:25.14	0.29	1.48	1.11	6426
58	J214812.8+473625	21:48:12.75	47:36:24.63	0.07	0.42	0.24	2862
59	J214842.8+472560	21:48:42.81	47:25:59.77	0.07	0.35	0.08	1044
60	J214846.1+472551	21:48:46.07	47:25:51.30	0.08	0.44	0.38	3150
61	J214846.1+472515	21:48:46.13	47:25:15.31	0.10	0.47	0.37	2943
62	J214852.0+473134	21:48:52.05	47:31:34.26	0.11	0.50	0.64	5553
63	J214854.8+472723	21:48:54.80	47:27:22.69	0.05	0.39	0.11	1647

Table 4
(Continued)

Clump[a] Number	Source Name[b] (MJLSG...)	R.A.[c] (J2000.0)	Decl.[c] (J2000.0)	Peak Flux[d] F_{850} (Jy/Bm)	Peak Flux[d] F_{450} (Jy/Bm)	Total Flux[d] S_{850} (Jy)	Area[d] A (arcsec^2)
64	J214856.3+473026	21:48:56.30	47:30:25.93	0.17	0.68	0.72	5112
65	J214923.5+472406	21:49:23.47	47:24:05.95	0.05	0.42	0.05	666
66	J214924.3+472851	21:49:24.26	47:28:51.06	0.27	0.94	1.43	7146
67	J214931.0+472607	21:49:30.99	47:26:06.99	0.07	0.49	0.25	2979
68	J214931.5+472725	21:49:31.48	47:27:25.06	0.14	0.66	0.74	3996
69	J214933.9+472710	21:49:33.86	47:27:10.39	0.18	0.71	0.65	3114
70	J214936.8+472711	21:49:36.82	47:27:10.78	0.10	0.49	0.27	1971
71	J215235.8+471314	21:52:35.75	47:13:13.99	0.05	0.47	0.12	1638
72	J215238.4+471438	21:52:38.38	47:14:38.08	0.18	0.96	0.58	4833
73	J215307.0+471521	21:53:06.95	47:15:20.85	0.17	0.67	1.76	7785
74	J215307.3+471424	21:53:07.25	47:14:23.86	0.12	0.65	0.39	2367
75	J215312.6+471457	21:53:12.55	47:14:56.95	0.21	0.84	2.38	8775
76	J215312.9+471136	21:53:12.87	47:11:35.96	0.06	0.45	0.17	2655
77	J215314.6+471621	21:53:14.60	47:16:20.99	0.18	0.73	2.05	9630
78	J215315.5+471821	21:53:15.46	47:18:21.00	0.08	0.54	0.39	3654
79	J215317.8+471939	21:53:17.81	47:19:39.03	0.11	0.65	1.17	7893
80	J215324.6+471730	21:53:24.61	47:17:30.11	0.08	0.50	0.24	2466
81	J215331.4+472203	21:53:31.38	47:22:03.17	0.17	0.91	1.59	7974
82	J215333.2+471415	21:53:33.17	47:14:15.18	0.24	0.86	1.46	6156
83	J215334.6+472057	21:53:34.63	47:20:57.18	0.18	0.80	2.66	9783
84	J215335.5+471727	21:53:35.52	47:17:27.19	0.16	0.67	0.55	2088
85	J215336.4+471506	21:53:36.41	47:15:06.19	0.07	0.45	0.23	1908
86	J215336.7+471903	21:53:36.70	47:19:03.19	0.32	1.29	1.33	5175
87	J215336.7+471415	21:53:36.71	47:14:15.19	0.10	0.71	0.30	2358
88	J215337.3+471736	21:53:37.29	47:17:36.19	0.14	0.63	1.12	4509
89	J215337.6+471948	21:53:37.58	47:19:48.19	0.31	1.16	1.82	6129
90	J215340.8+471527	21:53:40.83	47:15:27.20	0.05	0.43	0.17	2259
91	J215345.3+471357	21:53:45.25	47:13:57.20	0.05	0.50	0.10	1485
92	J215345.8+471736	21:53:45.84	47:17:36.20	0.10	0.60	0.49	3357
93	J215350.5+471233	21:53:50.55	47:12:33.18	0.10	0.69	0.91	6192
94	J215350.5+471348	21:53:50.55	47:13:48.18	0.21	0.94	1.74	5652
95	J215354.7+471321	21:53:54.67	47:13:21.16	0.21	0.95	1.51	5445
96	J215355.9+471354	21:53:55.85	47:13:54.15	0.20	0.91	1.39	6354

Notes.
[a] Clump observation designation.
[b] The source name is based on the coordinates of the peak emission location of each object in R.A. and decl.: Jhhmmss.s ± ddmmss.
[c] Peak position, at 850 μm, for each clump.
[d] Peak flux at 850 and 450 μm within the clump boundary, total flux at 850 μm within the clump boundary, and the area spanned by the clump.

Figures 2 and 3 use contours to show the clump boundaries within the two IC 5146 molecular cloud regions. Within the Cocoon Nebula, the majority of the clumps merge together to create a broken ring around the central star cluster while in the Northern Streamer, the clumps fan out along the known filaments uncovered by *Herschel* (Arzoumanian et al. 2011). In both regions, however, the distribution of clumps typically generate one-dimensional sequences and relatively straight filamentary chains.

Although the single most massive clump lies in the Northern Streamer, the typical clump in the Cocoon Nebula is about twice as massive (mean 11.5 $M_\odot$, median 6.6 $M_\odot$) as that found in the Northern Streamer (mean 6.5 $M_\odot$, median 3.2 $M_\odot$), assuming that the temperatures and dust properties are the same across all of IC 5146. Many of the clumps in IC 5146 are closely related to the YSOs, especially the Class 0 and I sources (see Section 4.3). Of the 70 clumps in the Northern Streamer (Clumps 1–70 in Table 4), 15 (21%) have at least one associated YSO. In contrast, of the 26 clumps observed in the Cocoon Nebula (Clumps 71–96), 14 (54%) harbour at least one YSO within their boundaries. At first glance, this suggests that star formation is more active in the Cocoon Nebula. It is also possible, however, that the earliest stage of star (clump) formation is ramping down in the Cocoon Nebula and therefore the majority of the remaining clumps are presently star-forming. In the Northern Streamer, a smaller fraction of clumps host embedded YSOs and almost all of the YSOs in the region are still heavily embedded in the dust continuum, implying an earlier evolutionary time (see also Section 4.3).

Although these clumps are likely to have additional non-thermal support, given their large size and mass, it is interesting to compare them against known static isothermal models, such as Bonnor–Ebert (BE) spheres (Ebert 1955; Bonnor 1956). BE sphere models denote a continuum of solutions for equilibrium self-gravitating isothermal spheres with external bounding pressure, from very-low-mass objects that have an almost constant density throughout to critical models that are on the very edge of gravitational collapse and have a large variation in density between the center and the edge. This continuum of models can be represented by a single observational measure,

Table 5
Derived Properties of the Identified 850 μm Clumps

Clump[a] Number	Total Mass[b] M_{850} ($M_\odot$)	Jeans Mass[b] M_J ($M_\odot$)	Clump Radius[b] R_c (parsec)	Concentration[b]	Total YSOs Contained[c]	Class0+I/Flat Contained[c]	Class II/III Near Peak[c]	Class0+I/Flat Near Peak[c]
1	1.77	5.24	0.13	0.71	0	0	0	0
2	1.60	4.91	0.12	0.78	0	0	0	0
3	0.98	3.82	0.09	0.68	0	0	0	0
4	10.40	7.70	0.19	0.88	2	1	0	1
5	3.65	5.84	0.14	0.69	0	0	0	0
6	3.50	6.32	0.16	0.76	1	1	0	1
7	3.08	5.95	0.15	0.70	0	0	0	0
8	23.67	9.56	0.23	0.85	3	2	0	2
9	0.95	3.33	0.08	0.64	0	0	0	0
10	0.75	2.79	0.07	0.72	0	0	0	0
11	4.71	4.53	0.11	0.66	0	0	0	0
12	6.26	6.04	0.15	0.78	1	1	0	1
13	16.21	8.08	0.20	0.63	0	0	0	0
14	1.77	4.19	0.10	0.71	0	0	0	0
15	1.71	3.86	0.09	0.74	0	0	0	0
16	3.25	5.12	0.13	0.63	0	0	0	0
17	4.17	5.37	0.13	0.72	1	1	0	1
18	5.69	7.62	0.19	0.76	0	0	0	0
19	2.27	4.39	0.11	0.65	0	0	0	0
20	2.73	5.28	0.13	0.69	0	0	0	0
21	14.10	7.89	0.19	0.88	1	1	0	1
22	3.00	5.40	0.13	0.64	0	0	0	0
23	3.85	5.83	0.14	0.70	0	0	0	0
24	1.15	3.91	0.10	0.73	0	0	0	0
25	3.14	5.01	0.12	0.72	0	0	0	0
26	5.79	6.38	0.16	0.67	1	1	0	1
27	6.72	6.51	0.16	0.67	0	0	0	0
28	1.81	4.80	0.12	0.69	0	0	0	0
29	1.21	4.11	0.10	0.74	0	0	0	0
30	11.05	8.15	0.20	0.76	1	1	0	1
31	3.64	5.30	0.13	0.75	0	0	0	0
32	1.38	3.82	0.09	0.67	0	0	0	0
33	3.86	6.50	0.16	0.72	0	0	0	0
34	2.92	6.34	0.16	0.72	0	0	0	0
35	4.28	6.95	0.17	0.70	0	0	0	0
36	5.11	7.13	0.18	0.71	0	0	0	0
37	3.68	7.10	0.17	0.76	0	0	0	0
38	3.21	6.20	0.15	0.69	0	0	0	0
39	1.24	3.67	0.09	0.70	0	0	0	0
40	2.01	3.55	0.09	0.64	0	0	0	0
41	8.67	7.83	0.19	0.71	1	1	0	1
42	15.20	11.03	0.27	0.78	1	1	0	0
43	2.72	5.39	0.13	0.64	1	0	0	0
44	6.96	7.58	0.19	0.67	0	0	0	0
45	1.05	3.59	0.09	0.61	0	0	0	0
46	8.78	6.69	0.16	0.71	0	0	0	0
47	116.36	15.44	0.38	0.83	5	4	0	2
48	8.15	5.99	0.15	0.71	0	0	0	0
49	2.94	5.90	0.14	0.69	0	0	0	0
50	1.32	4.19	0.10	0.71	0	0	0	0
51	1.99	5.08	0.12	0.71	0	0	0	0
52	10.31	6.92	0.17	0.73	2	0	0	0
53	2.35	5.35	0.13	0.70	0	0	0	0
54	0.61	3.06	0.08	0.71	0	0	0	0
55	3.13	5.82	0.14	0.73	0	0	0	0
56	3.69	5.68	0.14	0.63	1	1	0	0
57	12.51	8.48	0.21	0.85	1	1	0	1
58	2.66	5.66	0.14	0.71	0	0	0	0
59	0.88	3.42	0.08	0.74	0	0	0	0
60	4.29	5.94	0.15	0.65	0	0	0	0
61	4.16	5.74	0.14	0.71	0	0	0	0
62	7.23	7.88	0.19	0.75	0	0	0	0
63	1.19	4.29	0.11	0.70	0	0	0	0

Table 5
(Continued)

Clump[a] Number	Total Mass[b] M_{850} ($M_\odot$)	Jeans Mass[b] M_J ($M_\odot$)	Clump Radius[b] R_c (parsec)	Concentration[b]	Total YSOs Contained[c]	Class0+I/Flat Contained[c]	Class II/III Near Peak[c]	Class0+I/Flat Near Peak[c]
64	8.11	7.56	0.19	0.80	0	0	0	0
65	0.53	2.73	0.07	0.68	0	0	0	0
66	16.13	8.94	0.22	0.82	0	0	0	0
67	2.84	5.77	0.14	0.73	0	0	0	0
68	8.36	6.69	0.16	0.69	0	0	0	0
69	7.36	5.90	0.15	0.72	0	0	0	0
70	3.06	4.70	0.12	0.68	0	0	0	0
71	1.33	4.28	0.11	0.65	0	0	0	0
72	6.52	7.35	0.18	0.84	2	1	0	1
73	19.82	9.33	0.23	0.67	0	0	0	0
74	4.42	5.15	0.13	0.68	1	1	0	1
75	26.83	9.91	0.24	0.69	1	0	0	0
76	1.87	5.45	0.13	0.72	0	0	0	0
77	23.10	10.38	0.25	0.71	0	0	0	0
78	4.42	6.40	0.16	0.66	0	0	0	0
79	13.22	9.40	0.23	0.68	0	0	0	0
80	2.74	5.25	0.13	0.71	0	0	0	0
81	17.85	9.45	0.23	0.71	1	1	0	1
82	16.44	8.30	0.20	0.76	3	2	0	1
83	29.97	10.46	0.26	0.63	1	1	0	1
84	6.24	4.83	0.12	0.60	1	1	0	0
85	2.64	4.62	0.11	0.58	1	0	0	0
86	14.99	7.61	0.19	0.81	2	2	0	1
87	3.35	5.14	0.13	0.69	0	0	0	0
88	12.65	7.10	0.17	0.58	0	0	0	0
89	20.54	8.28	0.20	0.77	1	1	0	0
90	1.88	5.03	0.12	0.67	2	0	1	0
91	1.17	4.08	0.10	0.66	0	0	0	0
92	5.54	6.13	0.15	0.65	0	0	0	0
93	10.25	8.33	0.20	0.64	1	0	0	0
94	19.54	7.95	0.20	0.65	1	1	0	1
95	17.01	7.81	0.19	0.68	0	0	0	0
96	15.66	8.43	0.21	0.74	2	1	0	0

Notes.
[a] Clump observation designation.
[b] See the text for definitions.
[c] "Contained" refers to YSOs that reside within the clump boundary. "Near peak" refers to those YSOs that reside within 15″ of the clump's peak position.

the concentration parameter, as described by Johnstone et al. (2000) and Kirk et al. (2006):

$$C = 1 - \left(\frac{1.13\,B^2}{A}\right)\left(\frac{S_{850}}{F_{850}}\right), \quad (3)$$

where $B = 14.''6$ is the effective 850 μm JCMT beamsize (Dempsey et al. 2013). To be stable against collapse, isothermal clumps with concentrations above 0.72 require additional support mechanisms such as pressure from magnetic fields. The concentration for each of the clumps in IC 5146 is included in Table 5. The concentrations range from 0.58 to 0.88, with a mean value of 0.70. Thus, the typical submillimeter clump appears on the verge of gravo-thermal instability based on concentration. It is worth noting that this analysis does not depend on the inferred temperature or dust emissivity (see Equation (3)) but does require that these properties remain constant throughout the clump. Furthermore, the concentration parameter is sensitive to the derived radius of the clump and thus choosing lower surface brightness thresholds for clump boundaries is likely to result in larger derived concentrations. As a result, individual concentration values should be treated with caution while the variations in concentration between clumps and across ensembles of clumps provides indications of the varying importance of gravity and non-thermal properties.

For all of the clumps in IC 5146, we also compare the derived mass, using Equation (2), against the maximum (Jeans-critical) mass of a stable thermally supported sphere of the same size R_c following the strategy of Sadavoy et al. (2010) and assuming a gas temperature of 15 K consistent with that determined from the dust

$$M_J = 29\left(\frac{T}{15\ \mathrm{K}}\right)\left(\frac{R_c}{0.07\ \mathrm{pc}}\right)M_\odot. \quad (4)$$

As shown in Table 5, the range of Jeans masses, $2.7 < M_J/M_\odot < 15.4$, is significantly smaller than the range of clump masses M_{850}. Nevertheless, a majority of the observed clumps appear to be Jeans stable according to this criterion: i.e., 62 of 96 or 65% have $M_{850}/M_J < 1$, with a noticeable

Table 6
Spitzer Protostars: Flux and Extinction

YSO Index[a]	R.A.[b] (J2000.0)	Decl.[b] (J2000.0)	Class Type[c]	F_{850}[d] (Jy/Bm)	F_{450}[d] (Jy/Bm)	A_V[d] mag	Host[e] Clump	Nearest[e] Clump	Distance (arcsec)
1727	21:44:43.0	+47:46:43	0+I	0.323	0.99	3.72	4	4	2.8
1729	21:44:48.3	+47:44:59	0+I	0.059	0.39	5.41	6	6	2.1
1731	21:44:51.7	+47:40:44	0+I	0.119	0.34	7.28	8	8	13.1
1732	21:44:52.0	+47:40:30	0+I	0.386	1.41	7.43	8	8	2.4
1736	21:44:53.9	+47:45:43	0+I	−0.002	0.20	4.00	⋯	6	73.7
1737	21:44:57.0	+47:41:52	FLAT	0.047	0.00	5.41	12	12	12.1
1739	21:45:02.6	+47:33:07	0+I	0.102	0.00	1.80	17	17	6.0
1741	21:45:08.3	+47:33:05	FLAT	0.435	1.83	4.18	21	21	1.5
1742	21:45:27.8	+47:45:50	0+I	−0.019	−0.14	1.74	⋯	18	243.4
1743	21:45:31.2	+47:36:21	0+I	0.081	−0.07	1.63	26	26	5.5
1746	21:45:58.5	+47:36:01	0+I	0.126	0.31	14.23	30	30	2.6
1753	21:47:03.0	+47:33:14	0+I	0.034	0.16	8.70	42	42	35.8
1754	21:47:06.0	+47:39:39	0+I	0.074	0.34	4.22	41	41	4.1
1757	21:47:21.2	+47:32:26	FLAT	0.299	0.84	13.65	47	47	21.7
1758	21:47:22.6	+47:32:05	0+I	0.530	1.86	13.65	47	47	7.4
1759	21:47:22.7	+47:32:14	0+I	0.662	2.74	13.65	47	47	2.4
1760	21:47:28.7	+47:32:17	FLAT	0.124	0.46	11.47	47	52	22.1
1763	21:47:55.6	+47:37:11	0+I	0.046	0.10	4.45	56	56	30.3
1764	21:47:59.2	+47:36:26	0+I	0.246	1.22	3.54	57	57	1.3
1765	21:52:14.3	+47:14:54	0+I	0.004	−0.14	3.31	⋯	71	240.3
1776	21:52:37.7	+47:14:38	0+I	0.161	0.55	6.19	72	72	6.9
1788	21:53:06.9	+47:14:34	0+I	0.094	0.38	5.23	74	74	10.7
1798	21:53:25.0	+47:16:22	FLAT	0.004	0.10	5.22	⋯	80	68.2
1803	21:53:28.3	+47:15:43	0+I	−0.008	−0.04	5.52	⋯	85	90.4
1804	21:53:28.6	+47:15:51	0+I	0.003	0.18	5.52	⋯	85	91.3
1811	21:53:30.4	+47:13:10	FLAT	−0.002	0.18	5.02	⋯	82	71.0
1814	21:53:31.4	+47:22:17	0+I	0.088	0.34	4.26	81	81	13.8
1818	21:53:33.0	+47:14:39	FLAT	0.015	0.13	5.95	82	82	23.9
1820	21:53:33.1	+47:14:18	0+I	0.212	0.46	6.00	82	82	2.9
1823	21:53:33.9	+47:17:24	0+I	0.063	0.12	5.79	84	84	16.8
1826	21:53:34.7	+47:20:44	FLAT	0.173	0.68	5.06	83	83	13.2
1830	21:53:36.3	+47:19:03	0+I	0.243	0.62	6.08	86	86	4.1
1831	21:53:37.0	+47:18:17	0+I	0.039	−0.10	5.77	86	88	40.9
1833	21:53:38.3	+47:19:35	FLAT	0.229	0.67	5.94	89	89	15.1
1841	21:53:42.0	+47:14:26	FLAT	0.010	−0.10	6.72	⋯	91	43.9
1846	21:53:49.7	+47:13:51	0+I	0.135	0.24	7.20	94	94	9.1
1849	21:53:55.7	+47:20:30	0+I	0.019	−0.22	2.50	⋯	89	188.8
1851	21:53:58.1	+47:14:45	0+I	0.014	0.11	4.63	96	96	55.8

Notes.
[a] YSO observation designation from Dunham et al. (2015).
[b] Location of YSO.
[c] YSO Class (see the text).
[d] See text for definitions.
[e] Clump observation designation (see Table 3).

difference between the two regions. In the Northern Streamer, 51 of 70, or 73%, are stable by this criterion whereas in the Cocoon Nebula only 11 of 26, or 42%, appear to be stable. Furthermore, the subset of 29 clumps across IC 5146 harbouring embedded protostars show a propensity for instability, with 20 of 29, or 69%, having $M_{850}/M_J > 1$. The Jeans stability argument is extremely sensitive to the assumed temperature given that the Jeans mass increases and the dust continuum mass decreases with increasing temperature. Nevertheless, assuming that the properties of clumps are similar across IC 5146, the Jeans stability ratio (M_{850}/M_J) allows for an ordering of the importance of self-gravity within clumps, with the highest ratios denoting the most gravitationally unstable clumps.

4.3. Dust Continuum and YSOs

Spitzer observed the IC 5146 region (Harvey et al. 2008) and identified 131 YSOs within the SCUBA-2 areal coverage, classified as either Class 0/I (28), Flat (10), Class II (79), or Class III (14) (Dunham et al. 2015). Of these, 38 reside in the Northern Streamer, with 19 Class 0/I and Flat protostars versus 19 Class II+III more evolved YSOs. The Cocoon Nebula has 91 YSOs in total, divided into 19 Class 0/I and Flat protostars versus 74 Class II+IIIs. Tables 6 and 7 detail the location, the underlying 450 μm and 850 μm flux density, and the associated near-infrared extinction for *Spitzer* "protostars" (Class 0/I and Flat) and "evolved sources" (Class II+III), respectively. These tables also note the identifier of the clump in which each YSO resides as well as both the offset distance to the nearest clump

Table 7
Spitzer Evolved Sources: Flux and Extinction

YSO Index[a]	R.A.[b] (J2000.0)	Decl.[b] (J2000.0)	Class Type[c]	F_{850}[d] (Jy/Bm)	F_{450}[d] (Jy/Bm)	A_V[d] mag	Host[e] Clump	Nearest[e] Clump	Distance (arcsec)
1728	21:44:44.4	+47:46:49	II	0.070	0.08	3.72	4	4	18.0
1730	21:44:49.1	+47:46:21	II	0.003	−0.09	4.07	⋯	4	66.7
1733	21:44:52.3	+47:44:55	II	−0.009	0.06	3.85	⋯	6	42.0
1734	21:44:53.2	+47:46:07	II	0.004	−0.05	3.37	⋯	6	86.1
1735	21:44:53.4	+47:40:48	II	0.064	0.20	7.50	8	8	20.5
1738	21:45:01.5	+47:41:22	III	0.007	0.22	6.23	⋯	12	46.8
1740	21:45:02.9	+47:42:29	III	0.009	−0.21	4.49	⋯	12	58.9
1744	21:45:41.0	+47:37:07	II	−0.014	−0.00	3.81	⋯	28	103.3
1745	21:45:57.1	+47:19:31	II	−0.020	0.01	2.35	⋯	32	880.0
1747	21:46:05.7	+47:20:48	II	−0.004	−0.14	1.01	⋯	32	787.2
1748	21:46:22.0	+47:35:00	III	−0.009	−0.29	8.04	⋯	33	55.5
1749	21:46:26.6	+47:44:15	II	−0.006	0.05	2.15	⋯	37	361.9
1750	21:46:41.3	+47:34:31	II	−0.007	−0.06	5.86	⋯	36	87.7
1751	21:46:46.7	+47:35:55	III	−0.019	−0.08	3.31	⋯	36	92.2
1752	21:46:49.2	+47:45:08	III	−0.003	0.33	1.49	⋯	37	315.6
1755	21:47:10.8	+47:32:04	II	0.022	−0.05	14.19	43	43	20.0
1756	21:47:20.6	+47:32:03	II	0.381	1.33	13.65	47	47	24.4
1761	21:47:32.9	+47:32:08	II	0.041	0.12	10.98	52	52	27.5
1762	21:47:34.2	+47:32:05	II	0.016	−0.22	10.98	52	52	40.0
1766	21:52:19.2	+47:15:55	II	0.004	−0.02	4.15	⋯	72	209.8
1767	21:52:19.6	+47:14:38	II	−0.007	0.11	3.05	⋯	71	184.8
1768	21:52:30.7	+47:14:06	II	−0.000	−0.01	4.22	⋯	71	73.2
1769	21:52:32.6	+47:13:46	II	−0.005	0.17	4.15	⋯	71	45.4
1770	21:52:32.7	+47:14:09	II	−0.011	−0.03	4.15	⋯	71	63.2
1771	21:52:33.2	+47:10:50	II	0.008	−0.12	1.64	⋯	71	146.3
1772	21:52:34.0	+47:13:43	II	0.042	−0.56	4.02	⋯	71	34.1
1773	21:52:34.5	+47:14:40	II	0.005	0.31	5.31	⋯	72	39.5
1774	21:52:36.1	+47:11:56	II	0.003	−0.23	2.62	⋯	71	78.1
1775	21:52:36.5	+47:14:36	II	0.001	−0.11	6.19	72	72	19.2
1777	21:52:39.7	+47:11:10	III	−0.017	−0.04	2.77	⋯	71	130.3
1778	21:52:41.2	+47:12:52	II	0.021	−0.17	4.21	⋯	71	59.7
1779	21:52:42.7	+47:12:09	II	−0.001	0.17	3.86	⋯	71	96.1
1780	21:52:42.7	+47:10:13	II	−0.019	0.12	2.14	⋯	71	194.3
1781	21:52:45.4	+47:10:39	III	−0.002	0.14	2.55	⋯	71	183.5
1782	21:52:46.5	+47:12:49	II	0.009	0.02	4.37	⋯	71	112.3
1783	21:52:49.5	+47:12:17	II	0.026	0.00	4.02	⋯	71	151.2
1784	21:52:50.1	+47:12:20	II	−0.003	0.15	3.93	⋯	71	155.8
1785	21:52:57.0	+47:15:22	II	−0.009	−0.07	4.48	⋯	73	101.3
1786	21:52:59.1	+47:16:28	III	−0.001	−0.19	3.84	⋯	73	104.3
1787	21:53:03.9	+47:23:30	II	−0.005	0.24	2.79	⋯	79	270.8
1789	21:53:07.5	+47:24:44	II	0.023	−0.21	2.65	⋯	81	291.0
1790	21:53:08.4	+47:12:53	II	−0.008	0.02	3.77	⋯	76	89.5
1791	21:53:08.6	+47:12:47	II	−0.011	0.19	3.70	⋯	76	83.3
1792	21:53:18.4	+47:14:20	II	0.038	0.15	4.81	75	75	70.1
1793	21:53:20.3	+47:12:57	II	−0.000	−0.19	3.58	⋯	76	110.9
1794	21:53:22.6	+47:28:17	II	0.005	0.09	1.06	⋯	81	384.3
1795	21:53:22.7	+47:14:23	II	0.027	−0.06	4.31	⋯	82	107.0
1796	21:53:23.0	+47:14:08	II	0.013	−0.08	4.13	⋯	82	103.9
1797	21:53:24.9	+47:15:29	II	0.013	−0.05	4.95	⋯	82	112.0
1799	21:53:26.3	+47:15:43	II	0.004	0.01	4.95	⋯	80	108.5
1800	21:53:27.1	+47:16:58	III	−0.022	−0.08	4.89	⋯	80	40.9
1801	21:53:27.3	+47:14:50	II	0.005	0.23	5.01	⋯	82	69.2
1802	21:53:27.7	+47:15:11	III	−0.004	0.05	5.01	⋯	82	78.9
1805	21:53:28.8	+47:16:13	II	0.019	0.30	5.97	⋯	80	88.1
1806	21:53:28.9	+47:15:37	II	−0.009	−0.29	5.63	⋯	85	82.5
1807	21:53:28.9	+47:16:52	II	0.018	0.23	5.69	⋯	80	57.9
1808	21:53:29.6	+47:13:54	II	−0.006	−0.15	4.84	⋯	82	42.1
1809	21:53:30.2	+47:16:03	II	−0.020	−0.03	5.97	⋯	85	85.0
1810	21:53:30.3	+47:13:13	II	−0.013	−0.10	5.02	⋯	82	68.7
1812	21:53:30.5	+47:14:44	II	0.001	−0.04	5.12	⋯	82	39.7
1813	21:53:30.8	+47:16:06	II	−0.003	0.10	5.97	⋯	85	82.7
1815	21:53:31.6	+47:16:28	II	0.008	0.14	6.11	⋯	84	71.4
1816	21:53:31.8	+47:16:14	II	−0.010	−0.10	6.11	⋯	84	82.4

Table 7
(Continued)

YSO Index[a]	R.A.[b] (J2000.0)	Decl.[b] (J2000.0)	Class Type[c]	F_{850}[d] (Jy/Bm)	F_{450}[d] (Jy/Bm)	A_V[d] mag	Host[e] Clump	Nearest[e] Clump	Distance (arcsec)
1817	21:53:32.0	+47:16:03	II	−0.009	0.01	6.07	⋯	85	72.4
1819	21:53:33.0	+47:16:09	III	0.001	0.29	6.11	⋯	85	71.8
1821	21:53:33.2	+47:13:41	II	0.074	0.15	6.00	82	82	34.2
1822	21:53:33.4	+47:11:16	II	−0.013	0.01	5.85	⋯	82	179.2
1824	21:53:34.0	+47:15:55	II	−0.014	−0.16	6.11	⋯	85	54.6
1825	21:53:34.1	+47:16:04	III	−0.022	−0.21	6.11	⋯	85	62.4
1827	21:53:35.7	+47:12:26	III	0.020	0.12	7.00	⋯	87	109.7
1828	21:53:35.8	+47:12:12	II	0.009	0.03	7.00	⋯	87	123.5
1829	21:53:36.2	+47:10:27	II	−0.012	0.09	5.79	⋯	93	193.2
1832	21:53:38.2	+47:14:59	II	0.037	0.06	6.22	85	85	19.6
1834	21:53:38.4	+47:12:31	II	0.021	−0.11	7.47	⋯	87	105.6
1835	21:53:38.7	+47:12:05	II	0.004	0.02	7.32	⋯	93	124.0
1836	21:53:38.9	+47:13:27	II	−0.004	0.17	7.49	⋯	87	53.1
1837	21:53:40.0	+47:15:26	II	0.039	−0.06	5.61	90	90	8.6
1838	21:53:40.4	+47:15:08	II	0.031	0.08	6.22	90	90	19.7
1839	21:53:40.6	+47:16:49	II	−0.003	0.11	5.50	⋯	88	58.0
1840	21:53:40.8	+47:15:42	II	0.003	0.19	5.61	⋯	90	14.8
1842	21:53:42.1	+47:15:53	II	−0.009	−0.15	5.08	⋯	90	28.8
1843	21:53:42.5	+47:18:25	II	0.039	0.05	5.56	⋯	92	59.5
1844	21:53:45.2	+47:12:35	II	−0.000	0.24	5.81	93	93	54.5
1845	21:53:46.5	+47:14:35	II	0.021	0.05	6.38	⋯	91	39.9
1847	21:53:51.6	+47:16:48	II	−0.002	−0.06	4.06	⋯	92	75.9
1848	21:53:51.8	+47:07:11	III	−0.017	0.06	0.85	⋯	93	322.4
1850	21:53:57.9	+47:19:34	II	−0.018	0.02	2.82	⋯	92	170.0
1852	21:54:00.3	+47:25:22	II	0.020	−0.14	1.09	⋯	81	354.7
1853	21:54:01.4	+47:14:21	II	0.016	−0.10	4.91	96	96	62.5
1854	21:54:06.0	+47:22:05	II	0.005	−0.19	1.37	⋯	89	319.6
1855	21:54:08.7	+47:13:57	II	0.000	0.25	3.39	⋯	96	130.9
1856	21:54:12.5	+47:14:35	II	−0.023	−0.01	1.84	⋯	96	174.4
1857	21:54:18.7	+47:12:09	II	0.007	−0.07	1.43	⋯	95	255.2

Notes.
[a] YSO observation designation from Dunham et al. (2015).
[b] Location of YSO.
[c] YSO Class (see the text).
[d] See text for definitions.
[e] Clump observation designation (see Table 3).

peak and that clump-identifier. Even with the greater number of YSOs being in the Cocoon Nebula, only twenty (21%) of the YSOs are associated with clumps identified in the region (see also Figure 2). Broken down by type, twelve of the protostars (63%) and eight of the more-evolved YSOs (11%) are coincident with clumps. Alternatively, looking at the Northern Streamer, twenty-three YSOs (60%) are still within the observed clumps. This number can be broken down to seventeen protostars (89%) and six more-evolved sources (32%). Hence, independent of which evolutionary stage of YSO one compares the Northern Streamer appears to be less evolved than the Cocoon Nebula (see also Section 4.2).

Figure 4 compares the cumulative mass, as determined from the extinction map within the *Spitzer* footprint, to the emergence of these YSOs as a function of the underlying extinction. It is clear that the YSOs are at least as biased to higher extinction regions as the clump mass in the cloud, reinforcing the notion that stars form where there is significant material (e.g., Johnstone et al. 2004; Hatchell et al. 2005; Kirk et al. 2006; Könyves et al. 2013). Furthermore, a large fraction of the most embedded YSOs, the protostellar Class 0/I and Flat, are found at extreme extinctions of $A_V > 5$, which is also where the SCUBA-2-derived mass resides. The more-evolved Class II+III sources are the least biased toward high extinction. This progression of Classes against extinction in IC 5146 can be interpreted as an evolutionary sequence. The heavily embedded Class 0/I and Flat sources still reside near their natal material while the older Class II and Class III sources have had an opportunity to disperse or move away from their remnant birth sites.

Figure 5 shows and Tables 6 and 7 record the distribution of submillimeter flux densities associated with the position of each YSO from the 850 μm maps. Most of the Class II and Class III YSOs are associated with little to no submillimeter emission at either 450 μm or 850 μm. This result is as expected (Dunham et al. 2015) since those YSOs are more evolved, with small or non-existent surrounding envelopes and enough time has passed for them to have moved from their natal surroundings. The younger Class 0/I and Flat YSOs are seen to be embedded in regions of higher flux emission, appropriate for dense envelopes and/or proximity to material responsible for their birth. While there appear to be a subset of Class 0/I

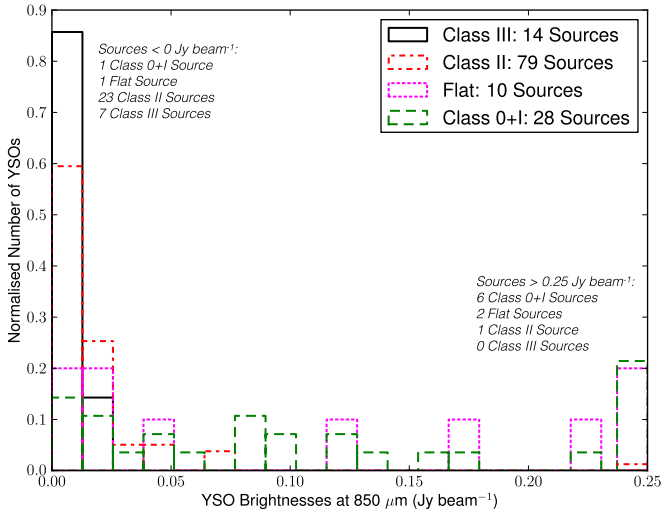

Figure 5. Histogram of the 850 μm SCUBA-2 flux at the position of *Spitzer* YSOs normalized for each class (highlighted as in the legend). All 131 sources can be found in Table 4.

and Flat YSOs without significant coincident submillimeter emission, it is likely that these sources have been mis-classified and are actually somewhat older. For example, Heiderman & Evans (2015) surveyed 546 such *Spitzer*-classified YSOs using $HCO^+(J = 3 - 2)$ and found that only 84% were bona fide young protostars. Additionally, using SCUBA-2 observations in Southern Orion A, Mairs et al. (2016) find a similar fraction of likely mis-identified Class 0/I and Flat sources.

Figure 6 shows the distribution of YSO angular offsets from clump peaks. The most deeply embedded Class 0/I YSOs are found to dominate the distribution at very small offsets, $d < 15''$ (1.4×10^3 au at a distance of 950 pc) roughly equivalent to the 850 μm beam. The roughly 25% of the Class 0/I's that are found at larger offsets from the clump peaks are likely mis-identified as discussed in the previous paragraph. Furthermore, the ten Flat spectrum YSOs are all found within 80″ of a clump peak while the Class II YSOs are predominantly found at intermediate offsets, $d < 150''$ (1.4×10^4 au), but with a very broad overall range. The few Class III sources are almost exclusively found at a similar intermediate offsets, $40'' < d < 180''$, although three lie further than 300″ away from any clump peak.

Detailed consideration of the physical properties of the clumps containing YSOs reveals a few important trends. Figure 7 shows histograms of the Jeans stability ratio for all 96 clumps, and just those with YSOs. Clumps harbouring YSOs within their boundary have a distribution of Jeans stability ratio that is skewed toward larger (more unstable) values and those harbouring a protostar near the peak makes this skew slightly more extreme. Figure 8 shows the Jeans stability versus the number of embedded YSOs. The degree of instability is in general larger for clumps that contain a greater number of embedded YSOs. Finally, Figure 9 shows histograms of concentration for all clumps and those with YSOs. Clumps across the entire range of observed concentrations contain YSOs, with YSO-harbouring clumps dominating both the low and high concentration ends of the distribution. Considering only those clumps with protostars close to their peaks, however, one finds an enhancement toward high concentration.

4.4. Clustering of Sources

Given that there are clear differences between the spatial distribution of the clumps and protostars in the Cocoon Nebula and the Northern Streamer, we have analyzed the clustering properties of these objects. We calculate the local surface density of clumps around each clump by using the separation to the Nth nearest neighbor, i.e.,

$$\sigma_N = \frac{N}{\pi r_N^2} \quad (5)$$

where σ_N is the local surface density, and r_N is the distance to the Nth nearest neighbor. The fractional uncertainty of the surface density is $N^{-0.5}$ (Casertano & Hut 1985; Gutermuth et al. 2009). Following Kirk et al. (2016b) and Lane et al. (2016), we calculate the surface density values for 5 and 10 nearest neighbors, finding no significant difference between the two approaches. We use a similar approach to calculate the local surface density for each protostar. For the protostar calculation, we consider the Class 0/I and Flat sources as a single group and the Class II sources as a second group, using only the distances to other sources in the same group for the surface density calculation, i.e., the Class II measurement only considers the distances between Class II sources.

Figure 10 shows the distributions of the surface densities derived for sources in the Cocoon Nebula and Northern Streamer separately. The most obvious difference between the two subregions is in the protostellar surface densities, with protostars in the Cocoon Nebula showing much stronger signs of clustering than the Northern Streamer, confirming the visual impression of the two regions. Clumps in the Cocoon Nebula also appear to have a slight tendency to lie closer together than in the Northern Streamer, though this is less visually apparent. We ran two-sided Kolmogorov–Smirnov tests on the two distributions, and found probabilities of 8% or less that the Cocoon and Streamer populations are drawn from the same parent sample (0.45%, 0.06%, and 8% for the clumps, Class 0/I/Flat and Class II sources respectively). We also ran a Mann-Whitney test to examine the probability that sources in the Cocoon tend to have higher surface densities than sources in the Streamer and find significant probabilities for the clumps and Class 0/I/Flat sources (probabilities are 99.99%, 98%, and 87% for the clumps, Class 0/I/Flat, and Class II sources, respectively).

Following Kirk et al. (2016b) and Lane et al. (2016), we use a second clustering measurement adapted from protostellar analysis in simulations by Maschberger & Clarke (2011), and we compare the local surface density of clumps to their total flux. In the Orion A and B molecular clouds, Lane et al. (2016) and Kirk et al. (2016b) found strong evidence of a tendency for higher flux sources to inhabit locally higher surface density environments, which was interpreted, in combination with other lines of evidence, as a sign of dense core mass segregation in those clouds. We run a similar comparison here. Figure 11 shows the local surface density and flux for the clumps in IC 5146. We analyze both the full sample of clumps, and separately, only the clumps in the Northern Streamer. We did not expect to see signs of mass segregation within the Cocoon Nebula, given that the clumps are roughly arranged in a ring around the protostellar cluster, suggesting that the region is more evolved, and that the submillimeter clumps may represent a second round of star formation. Even if mass

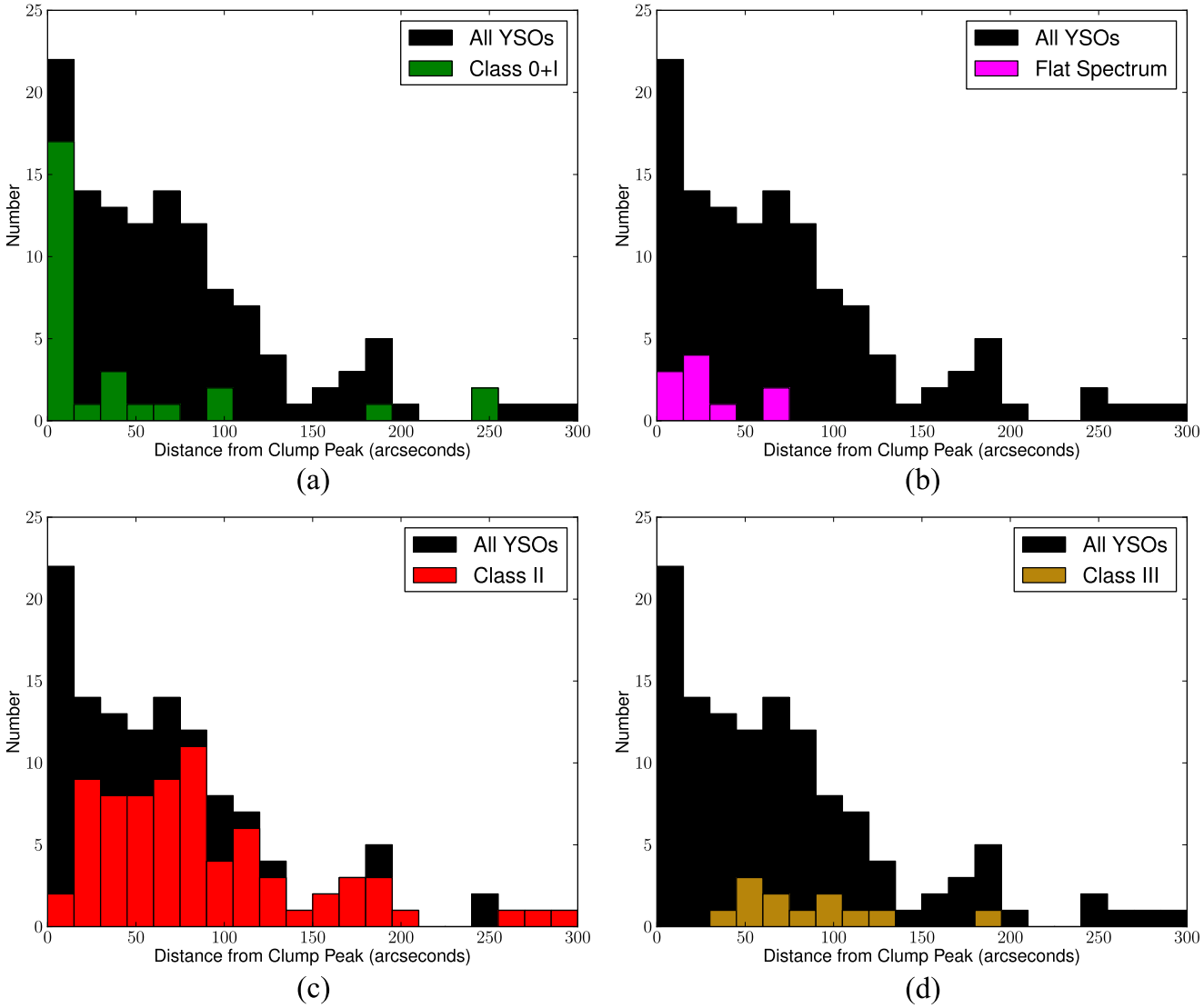

Figure 6. Histograms of YSO angular offset from nearest clump peak. In all panels, black represents the entire sample of YSOs within 300″ of a clump peak. (a) Offsets for Class 0/I sources (Green). (b) Offsets for FLAT sources (Pink). (c) Offsets for Class II sources (Red). (d) Offsets for Class III sources (Gold). See the text for details on YSO class determination.

segregation were present, the ring-like geometry of the clumps would make it difficult to measure in the Cocoon Nebula. Even removing the Cocoon Nebula sources, however, we see no signs of a trend of increasing local surface density with higher flux clumps. Kirk et al. (2016b) and Lane et al. (2016) ran their analysis considering both the full sample of dense cores in Orion and also only the starless cores, since the presence of a protostar could imply a higher temperature, thus increasing the flux of a dense core without also implying an increased mass. No trend is seen in Figure 11 for either the full set of clumps or only starless clumps within the Northern Streamer. To highlight this lack of a trend, we also show the co-moving mean surface density values for both the full set of IC 5146 clumps and the starless clumps within the Northern Streamer, using a smoothing window width of 20 clumps.

The lack of support for the presence of mass segregation within the Northern Streamer is surprising, given the strong signs of core mass segregation found in the Orion A and B molecular clouds using a similar analysis and identical observing technique with the JCMT. There are two possible explanations for the different behavior in IC 5146. First, mass segregation in dense cores and clumps may not be universal, but might be restricted only to the most clustered systems like Orion. This suggestion can soon be tested using the data available for other clouds observed by the JCMT GBS team. A second possibility is that the difference is due to the much larger distance to IC 5146 than Orion (and other GBS clouds). At the adopted 950 pc, IC 5146 is too distant to resolve individual dense cores, and we instead are only sensitive to the larger clump emission structures. The local surface density values derived for the clumps already suggest that we may be missing important details in unresolved substructures. Within the starless clumps in the Northern Streamer, the range of local surface densities is 0.49 $pc^{-2} \leqslant \sigma_{10} \leqslant 2.7$ pc^{-2}, a factor of only 5.5. In Orion A, Lane et al. (2016) find a range in surface densities of more than a factor of 100, and in Orion B, the range is about a factor of 60. In IC 5146, the mean clump radius is 0.15 pc, whereas in Orion A and B, the FellWalker-

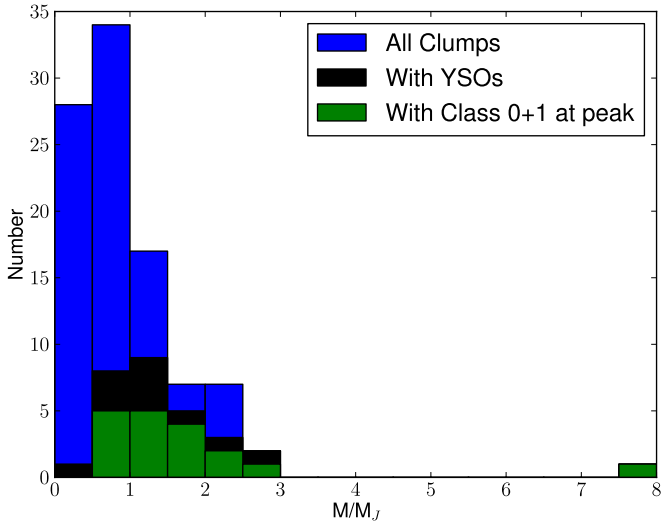

Figure 7. Histogram showing the Jeans stability, M/M_J, for all 96 clumps, the subset of 29 clumps that harbour YSOs, and the subset with protostars near their peak. The fraction of clumps harbouring YSO increases with M/M_J. Of the clumps harbouring YSOs, the fraction with protostars located near the clump centre increases as well with M/M_J.

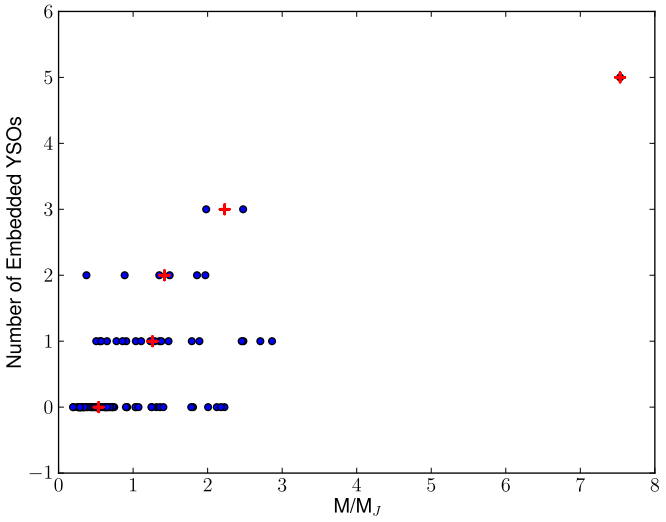

Figure 8. Scatter diagram for clumps showing the Jeans stability measure, M/M_J, vs. the number of embedded YSOs. Denoted by a red plus sign are the median M/M_J as a function of embedded YSOs. There is a clear relation revealed, with clumps that harbour a greater number of YSOs also having a larger median M/M_J.

based dense cores have mean effective radii of 0.06 pc. The filamentary geometry of the Northern Streamer may also make it more difficult to measure clustering properties, however, the recent work by Nunes et al. (2016) suggests that with sufficient resolution, clusters of dense cores might be expected. Using *WISE* data, Nunes et al. (2016) identify five new candidate protostellar clusters in the area around the Northern Streamer. Three of these, NBB 2, 3, and 4, all lie within areas we mapped with SCUBA-2, and two of these, NBB 2 and 4, lie close to each of the two brightest submillimeter clumps within this area.

It will be important to measure the clustering properties in other nearby molecular clouds to test whether IC 5146 appears different merely because of its distance.

5. Discussion

The contrast between the Cocoon Nebula and the Northern Streamer is evident throughout this analysis, revealing the large variation in structure and star formation that can arise within a single molecular cloud. Both regions show clear fragmentation of bright submillimeter emission into dense clumps with a similar fraction of the extinction-derived mass observable at 850 μm (5% for the Cocoon Nebula versus 4% for the Northern Streamer). The Northern Streamer, seen in extinction as a network of parallel filaments, breaks into chains of clumps when observed in the submillimeter. While only a small fraction of these clumps host YSOs, the majority of YSOs in the region lie within the clumps. The Cocoon Nebula, in contrast, appears more as a broken, fragmented ring surrounding a cluster of predominantly Class II protostars. A large fraction of these Cocoon Nebula clump fragments host YSOs but only a small fraction of the YSO population remains embedded within clumps. This analysis is independent of the YSO evolutionary stage.

The Cocoon Nebula is situated at the eastern end of the Northern Streamer and thus we theorize that it is a more-evolved portion of IC 5146, having produced 65 Class II YSOs versus the 14 Class II YSOs found in the Northern Streamer. The number of Class 0/I and Flat sources is identical between

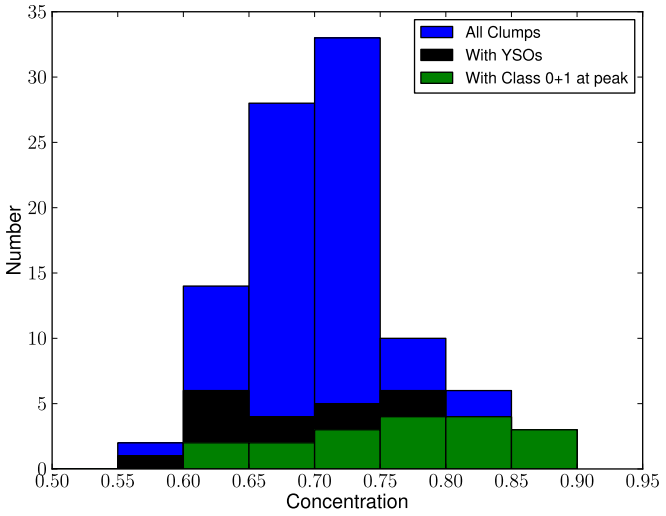

Figure 9. Histogram showing the concentration measure (Equation (3)) for all 96 clumps, as well as the subset of 29 clumps that harbour YSOs and those 18 with protostars near their peak. Although clumps embedded YSOs span the entire range of concentration, the clumps with higher concentration are most likely to have protostars near their peak.

the two regions despite the Northern Streamer containing twice the total extinction-derived mass of the Cocoon Nebula and almost three times as many submillimeter clumps. The variation in evolutionary age between the two regions may be due to the more localized mass concentration in the Cocoon Nebula, suggesting a higher initial density leading to a faster collapse. Alternatively, it might simply be due to the known enhanced gravitational instability produced at the ends of cylindrical structures (Pon et al. 2011, 2012), assuming that the entire IC 5146 might have begun as a single, elongated entity.

Early in its existence, the Cocoon Nebula developed a blister cavity due to the massive star BD+46° 3474, evacuating the central region and spreading material outward. This energetic event appears to have compressed the remaining clumps into a ring and triggered a second round of star formation, perhaps

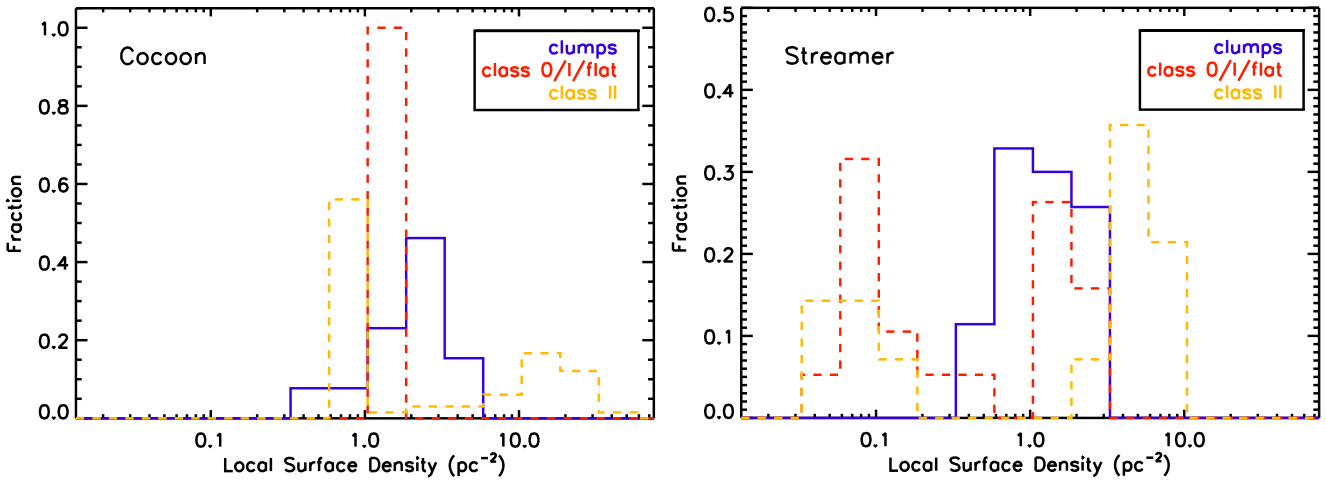

Figure 10. Distribution of local source surface densities derived for the Cocoon Nebula (left) and the Northern Streamer (right). In each panel, the solid blue line shows the clumps, while the dashed red line shows the Class 0/I and flat protostars and the dashed yellow line shows the Class II protostars. Results are plotted here for surface densities calculated using the ten nearest neighbors; using instead the five nearest neighbors gives a similar result.

explaining the high fraction of current clumps in the Cocoon with embedded YSOs. As suggested by the collect and collapse model (Whitworth et al. 1994), the compression may also explain the higher clump masses observed in the Cocoon Nebula, though there is only a modest difference in the mean densities within the Cocoon Nebula versus the Northern Streamer, 410 $M_{\odot}$ pc^{-3} versus 350 $M_{\odot}$ pc^{-3} respectively. Less clear is an explanation for the almost constant fraction of extinction-derived mass observed at 850 μm across both the Cocoon Nebula and the Northern Streamer. If this fraction traces clump formation efficiency then one might naively expect that the recent compression in the Cocoon Nebula should result in a higher fractional value than that found in the Northern Streamer. Alternatively, if star formation is ramping down in the Cocoon Nebula then the anticipated fractional value would be lower than in the Northern Streamer as more of the dense gas has been locked into stars or disrupted. Perhaps the similarity in the dense gas fraction is due to a combination of these two effects, with the enhancement and dispersal roughly cancelling out.

The Northern Streamer, conversely, has relatively few of the Class II YSOs (18%) despite being surrounded by 67% of the extinction-derived mass of the entire IC 5146 cloud and accounting for 57% of the submillimeter-derived mass. This suggests that star formation has not yet ramped up to the level found in the Cocoon Nebula. The lower mean (and median) masses for the clumps in the Northern Streamer may also be evidence of youth. Nevertheless, both the Jeans mass and concentration measures for the clumps in the Northern Streamer suggest that it is poised for significant star-formation activity continuing into the future. One additional indirect piece of evidence that star formation is only now ramping up in the Northern Streamer is found in the nature of Clump 47 and its nearby environment. Found near the eastern end of one of the Northern Streamer filaments, Clump 47 is the single most massive clump observed in the IC 5146 region. It is extremely Jeans unstable, assuming only thermal pressure support, and hosts a small ensemble of protostars already. The conditions within this clump may be similar, though scaled down, from those assumed to have led to the blister H II region associated with the Cocoon Nebula, including the notion that gravitational instabilities are associated with the ends of filaments.

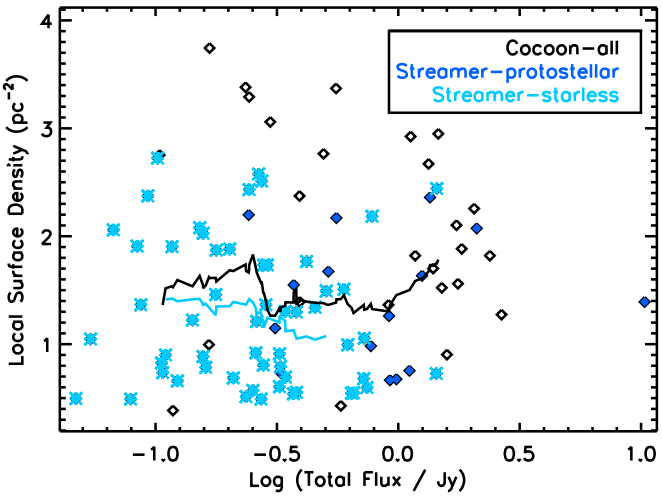

Figure 11. Comparison of the total flux and local surface densities of the clumps in IC 5146. Northern Streamer protostellar clumps are shown in dark blue filled diamonds while the starless clumps are shown in light blue asterisks. The solid black and light blue lines show the co-moving window mean values of the surface density for the full sample (black) and the starless clumps in the Northern Streamer only (light blue). No clear trend is seen between the surface density and clump total flux.

6. Summary

In this paper, we have presented a first look at IC 5146 from JCMT SCUBA-2 dust continuum data. We are able to confirm a number of key properties regarding IC 5146 as listed below.

1. The Cocoon Nebula is a site of spherical, clustered star formation that was disrupted by the energetic outflows of the massive BD+46° 3474. The 850 μm emission observed in this region shows a shell-like geometry around the central cavity and the clumps are often found to harbour protostars, suggesting vigorous but non-sustainable star formation. The Northern Streamer in contrast is an elongated network of near-parallel filamentary structure undergoing modest star-formation activity. Both regions reveal fragmentation of the denser material, leading to localized sites of star formation.

2. Dense clumps are associated with regions of high extinction, with over 50% of the submillimeter emission observed by SCUBA-2 in regions of high extinction ($A_V > 5$). The total estimate of the extinction-derived mass is $\sim$15600 $M_\odot$, whereas the SCUBA-2 dust continuum mass is only $\sim$630 $M_\odot$. Both subregions within IC 5146 have converted approximately the same fraction of extinction-derived mass into submillimeter-visible mass.
3. Using the FellWalker clump-finding algorithm, 96 clumps are identified in a mass range of 0.5–120 $M_\odot$. A majority of the clumps are found to be Jeans stable and one-third are found to harbour YSOs. Those clumps that harbour protostars are typically the most Jeans unstable. Furthermore, the clumps in the Cocoon Nebula are both more massive and more Jeans unstable.
4. In general, the YSOs and submillimeter dust emission are both found to be strongly associated with the higher extinction regions within the cloud. Younger YSOs, Class 0/I and Flat, are found closer to the centres of clumps and at higher submillimeter flux density levels than the more-evolved Class II and Class III objects.

We thank the anonymous referee for constructive comments that added to the clarity of the paper. We also thank Laurent Cambrésy for providing the extinction data used in this analysis and Michael Dunham for allowing us to utilize his accumulated *Spitzer* catalog information on the IC 5146 region (Dunham et al. 2015) before publication. Doug Johnstone is supported by the National Research Council of Canada and by an NSERC Discovery Grant. Steve Mairs was partially supported by the Natural Sciences and Engineering Research Council (NSERC) of Canada graduate scholarship program. S.C., D.J., and H.K. thank Herzberg Astronomy and Astrophysics at the National Research Council of Canada for making this project possible through their co-op program.

The authors wish to recognize and acknowledge the very significant cultural role and reverence that the summit of Maunakea has always had within the indigenous Hawaiian community. We are most fortunate to have the opportunity to conduct observations from this mountain. The JCMT has historically been operated by the Joint Astronomy Centre on behalf of the Science and Technology Facilities Council of the United Kingdom, the National Research Council of Canada and the Netherlands Organisation for Scientific Research. Additional funds for the construction of SCUBA-2 were provided by the Canada Foundation for Innovation. The identification number for the programme under which the SCUBA-2 data used in this paper is MJLSG36. The authors thank the JCMT staff for their support of the GBS team in data collection and reduction efforts. The Starlink software (Currie et al. 2014) is supported by the East Asian Observatory. These data were reduced using a development version from 2014 December (version 516b455a). This research has made use of NASA's Astrophysics Data System and the facilities of the Canadian Astronomy Data Centre operated by the National Research Council of Canada with the support of the Canadian Space Agency. This research used the services of the Canadian Advanced Network for Astronomy Research (CANFAR), which in turn is supported by CANARIE, Compute Canada, University of Victoria, the National Research Council of Canada, and the Canadian Space Agency. This publication makes use of data products from the 2MASS, which is a joint project of the University of Massachusetts and the Infrared Processing and Analysis Center/California Institute of Technology, funded by the National Aeronautics and Space Administration and the National Science Foundation. This research makes use of APLpy, an open-source plotting package for Python hosted at http://aplpy.github.com (Robitaille & Bressert 2012), and MATPLOTLIB, a 2D plotting library for Python (Hunter 2007).

Facility: JCMT (SCUBA-2).

Software: IRAF, Starlink (Currie et al. 2014), SMURF (Jenness et al. 2013; Chapin et al. 2013a, 2013b), CUPID (Berry et al. 2007, 2013), APLpy, Matplotlib.

Appendix A
Investigation into the Dust Temperature in IC 5146

The temperature of the dust within IC 5146 can be estimated by comparing the flux density emitted at 450 and 850 μm. A careful comparison requires not only consideration of the differing beamsizes at each wavelength, but also proper treatment of the full beam profile, which, for the JCMT, includes a significant amount of flux in the "secondary" beam at 450 μm (Di Francesco et al. 2008; Dempsey et al. 2013). Using the procedure outlined in Pattle et al. (2015) and Rumble et al. (2015), D. Rumble et al. (2017, in preparation) compiled temperature estimates for all of the GBS clouds based on the Legacy Release 1 reductions (see Section 3.1 and Mairs et al. 2015). Here, we examine the temperature map derived for IC 5146 to determine whether or not our assumption of a constant temperature of 15 K for the clumps is reasonable.

The D. Rumble et al. (2017, in preparation) temperature maps exclude pixels for which the value derived for the temperature is less than or equal to the error estimated for that temperature. Since much of the area observed in IC 5146 has relatively low flux densities, particularly at 450 μm, a large fraction of the map does not have reliable temperature estimates. We first examine all pixels in the temperature map where a temperature is measured. From this analysis, we find a mean temperature of 14 ± 5 K. Temperatures are similar for both the Northern Streamer and Cocoon Nebula subregions, with mean temperatures of 14 ± 5 K and 14 ± 6 K in the former and latter regions, respectively. Of the pixels with measureable temperatures, roughly 40% lie in the Northern Streamer and 60% lie in the Cocoon Nebula.

We next examine the temperature estimates at the locations of the clumps (see Section 4.2). Using either the average temperature across the clump, or only the temperature at the location of the peak 850 μm flux density, we find that the clump dust has a similar temperature to the region-wide measures above. The mean temperature of clumps calculated using the full clump extent is 14 ± 3 K, while the mean temperature of clumps using the temperature only at the clump peak is 13 ± 2 K. There is no significant difference in these values if the clumps are considered separately within the Northern Streamer and Cocoon Nebula regions. This is consistent with the recent work of D. Rumble et al. (2017, in preparation) that finds that young stars only provide significant heating of their surroundings when their spectral types are earlier than B.

Given the similarity in all of these temperature measures, we argue that it is reasonable to adopt a constant value of 15 K for the bulk of our analysis.

Table 8
CO Contamination of Clumps

Clump[a]	$F_{\rm area}$[b]	$f_{\rm CO,tot}$[c]	$f_{\rm CO,pk}$[c]
25	0.301	0.020	0.000
26	0.743	0.060	0.074
27	1.000	0.031	0.028
28	0.026	0.001	0.000
30	1.000	0.043	0.061
31	1.000	0.031	0.030
32	1.000	0.017	0.025
33	1.000	0.017	0.004
34	1.000	−0.020	−0.004
35	1.000	−0.003	0.018
36	1.000	0.019	−0.000
38	1.000	−0.011	−0.022
40	1.000	0.011	0.022
42	1.000	−0.008	0.005
43	1.000	0.036	−0.000
45	1.000	−0.016	−0.005
46	1.000	0.005	0.004
47	1.000	0.069	0.045
48	0.399	0.026	0.006
50	0.782	0.094	0.049
52	0.897	0.031	−0.002

Notes.
[a] Clump designation, as in Table 3.
[b] Fraction of area of clump where CO was mapped.
[c] Fraction of clump's total flux and peak flux attributable to CO contamination.

Appendix B
Investigation Into CO Contamination of the 850 μm Flux in IC 5146

A portion of the IC 5146 Northern Streamer, roughly 0.03 square degrees, was observed in ^{12}CO($J = 3 - 2$) using HARP (Buckle et al. 2010). The ^{12}CO($J = 3 - 2$) emission line lies within the SCUBA-2 850 μm bandpass, and can therefore "contaminate" the thermal dust emission measured (Johnstone et al. 2003; Drabek et al. 2012). Previous observations suggest that the amount of CO contamination is generally small, typically less than 20% (Johnstone et al. 2003; Drabek et al. 2012; Hatchell et al. 2013; Sadavoy et al. 2013; Buckle et al. 2015; Pattle et al. 2015; Salji et al. 2015a; Coudé et al. 2016; Kirk et al. 2016a), though in zones with weak 850 μm emission and a strong CO outflow, CO has been observed to contribute up to 90% of the flux.

We follow the procedure outlined in Drabek et al. (2012) to estimate the level of CO contamination where suitable observations exist within IC 5146. First, the ^{12}CO ($J = 3 - 2$) HARP observations were reduced using ORAC-DR (Jenness et al. 2015). Next, we re-ran the SCUBA-2 map-making data reduction process with the integrated CO intensity subtracted from the 850 μm emission seen in each raw data file, after scaling the CO integrated intensity based on the atmospheric transmission at the time of the observation. Finally, we mosaicked the CO-subtracted maps together and compared the resultant image with the original 850 μm mosaic.

The fractional CO contamination level is given by

$$f_{\rm CO} = \frac{S_{850,\rm orig} - S_{850,\rm noco}}{S_{850,\rm orig}} \quad (6)$$

where $S_{850,\rm orig}$ is the flux in the original 850 μm map and $S_{850,\rm noco}$ is the flux in the CO-subtracted 850 μm map. Using the clump boundaries identified with FellWalker (Section 4.2), we calculate the amount of CO contamination for each of the clumps where CO observations exist over at least part of their extent. Table 8 reports the CO contamination both for the total flux of each clump as well as the peak flux, in addition to the fraction of the clump area in which CO was observed. As can be seen from Table 8, the CO contamination is never higher than 10% and is often closer to 1%. For the fainter clumps, the CO contamination level is smaller than the pixel-to-pixel noise level, as is apparent by several values of negative contamination reported.

References

Arzoumanian, D., André, P., Didelon, P., et al. 2011, A&A, 529, L6
Berry, D. S. 2015, A&C, 10, 22
Berry, D. S., Reinhold, K., Jenness, T., & Economou, F. 2007, in ASP Conf. Ser. 376, Astronomical Data Analysis Software and Systems XVI, ed. R. A. Shaw, F. Hill, & D. J. Bell (San Francisco, CA: ASP), 425
Berry, D. S., Reinhold, K., Jenness, T., & Economou, F. 2013, CUPID: Clump Identification and Analysis Package, Astrophysics Source Code Library, ascl:1311.007
Bonnor, W. B. 1956, MNRAS, 116, 351
Broekhoven-Fiene, H., Matthews, B., Harvey, P., et al. 2016, ApJ, submitted
Buckle, J. V., Curtis, E. I., Roberts, J. F., et al. 2010, MNRAS, 401, 204
Buckle, J. V., Drabek-Maunder, E., Greaves, J., et al. 2015, MNRAS, 449, 2472
Cambrésy, L. 1999, A&A, 345, 965
Cambrésy, L., Beichman, C. A., Jarrett, T. H., & Cutri, R. M. 2002, AJ, 123, 2559
Casertano, S., & Hut, P. 1985, ApJ, 298, 80
Chapin, E., Gibb, A. G., Jenness, T., et al. 2013a, StaUN, 258
Chapin, E. L., Berry, D. S., Gibb, A. G., et al. 2013b, MNRAS, 430, 2545
Chen, M. C.-Y., Di Francesco, J., Johnstone, D., et al. 2016, ApJ, 826, 95
Coudé, S., Bastien, P., Kirk, H., et al. 2016, MNRAS, 457, 2139
Currie, M. J., Berry, D. S., Jenness, T., et al. 2014, in ASP Conf. Ser. 485, Astronomical Data Analysis Software and Systems XXIII, ed. N. Manset & P. Forshay (San Francisco, CA: ASP), 391
Dempsey, J. T., Friberg, P., Jenness, T., et al. 2013, MNRAS, 430, 2534
Di Francesco, J. 2012, in Astronomical Society of India Conf. Vol. 2, New insights into the earliest phases of low-mass star formation with the Herschel Space Observatory, 13
Di Francesco, J., Johnstone, D., Kirk, H., MacKenzie, T., & Ledwosinska, E. 2008, ApJS, 175, 277
Dobashi, K., Onishi, T., Iwata, T., et al. 1993, AJ, 105, 1487
Dobashi, K., Yonekura, Y., & Hayashi, Y. 2001, PASJ, 53, 811
Dobashi, K., Yonekura, Y., Mizuno, A., & Fukui, Y. 1992, AJ, 104, 1525
Drabek, E., Hatchell, J., Friberg, P., et al. 2012, MNRAS, 426, 23
Dunham, M. M., Allen, L. E., Evans, N. J., II, et al. 2015, ApJS, 220, 11
Ebert, R. 1955, ZAp, 37, 217
Elias, J. H. 1978, ApJ, 223, 859
Enoch, M. L., Glenn, J., Evans, N. J., II, et al. 2007, ApJ, 666, 982
Enoch, M. L., Young, K. E., Glenn, J., et al. 2006, ApJ, 638, 293
Evans, N. J., II, Dunham, M. M., Jørgensen, J. K., et al. 2009, ApJS, 181, 321
Forte, J. C., & Orsatti, A. M. 1984, ApJS, 56, 211
Gutermuth, R. A., Megeath, S. T., Myers, P. C., et al. 2009, ApJS, 184, 18
Harvey, P. M., Huard, T. L., Jørgensen, J. K., et al. 2008, ApJ, 680, 495
Hatchell, J., Richer, J. S., Fuller, G. A., et al. 2005, A&A, 440, 151
Hatchell, J., Wilson, T., Drabek, E., et al. 2013, MNRAS, 429, L10
Heiderman, A., & Evans, N. J., II 2015, ApJ, 806, 231
Herbig, G. H., & Dahm, S. E. 2002, AJ, 123, 304
Herbig, G. H., & Reipurth, B. 2008, in Handbook of Star Forming Regions, Vol. I: The Northern Sky ASP Monograph Publications, Vol. 4, Young Stars and Molecular Clouds in the IC 5146 Region, ed. B. Reipurth (San Francisco, CA: ASP), 108
Hildebrand, R. H. 1983, QJRAS, 24, 267
Holland, W., MacIntosh, M., Fairley, A., et al. 2006, Proc. SPIE, 6275, 62751E
Holland, W. S., Bintley, D., Chapin, E. L., et al. 2013, MNRAS, 430, 2513
Holland, W. S., Robson, E. I., Gear, W. K., et al. 1999, MNRAS, 303, 659
Hunter, J. D. 2007, CSE, 9, 90
Israel, F. P. 1977, A&A, 60, 233

Jenness, T., Chapin, E. L., Berry, D. S., et al. 2013, SMURF: SubMillimeter User Reduction Facility, Astrophysics Source Code Library, ascl:1310.007
Jenness, T., Currie, M. J., Tilanus, R. P. J., et al. 2015, MNRAS, 453, 73
Jenness, T., Stevens, J. A., Archibald, E. N., et al. 2002, MNRAS, 336, 14
Johnstone, D., Boonman, A. M. S., & van Dishoeck, E. F. 2003, A&A, 412, 157
Johnstone, D., Di Francesco, J., & Kirk, H. 2004, ApJL, 611, L45
Johnstone, D., Wilson, C. D., Moriarty-Schieven, G., et al. 2000, ApJ, 545, 327
Kackley, R., Scott, D., Chapin, E., & Friberg, P. 2010, Proc. SPIE, 7740, 1
Kauffmann, J., Bertoldi, F., Bourke, T. L., Evans, N. J., II, & Lee, C. W. 2008, A&A, 487, 993
Kirk, H., Di Francesco, J., Johnstone, D., et al. 2016a, ApJ, 817, 167
Kirk, H., Johnstone, D., & Di Francesco, J. 2006, ApJ, 646, 1009
Kirk, H., Johnstone, D., Di Francesco, J., et al. 2016b, ApJ, 821, 98
Könyves, V., André, P., Men'shchikov, A., et al. 2015, A&A, 584, A91
Könyves, V., André, P., Schneider, N., et al. 2013, AN, 334, 908
Kramer, C., Richer, J., Mookerjea, B., Alves, J., & Lada, C. 2003, A&A, 399, 1073
Lada, C. J., Alves, J., & Lada, E. A. 1999, ApJ, 512, 250
Lane, J., Kirk, H., Johnstone, D., et al. 2016, ApJ, 833, 44
Mairs, S., Johnstone, D., Kirk, H., et al. 2015, MNRAS, 454, 2557
Mairs, S., Johnstone, D., Kirk, H., et al. 2016, MNRAS, 461, 4022
Mairs, S., Johnstone, D., Offner, S. S. R., & Schnee, S. 2014, ApJ, 783, 60
Maschberger, T., & Clarke, C. J. 2011, MNRAS, 416, 541
Nunes, N. A., Bonatto, C., & Bica, E. 2016, Ap&SS, 361, 64
Onishi, T., Mizuno, A., Kawamura, A., Ogawa, H., & Fukui, Y. 1998, ApJ, 502, 296
Pattle, K., Ward-Thompson, D., Kirk, J. M., et al. 2015, MNRAS, 450, 1094
Polychroni, D., Schisano, E., Elia, D., et al. 2013, ApJL, 777, L33
Pon, A., Johnstone, D., & Heitsch, F. 2011, ApJ, 740, 88
Pon, A., Toalá, J. A., Johnstone, D., et al. 2012, ApJ, 756, 145
Robitaille, T., & Bressert, E. 2012, APLpy: Astronomical Plotting Library in Python, Astrophysics Source Code Library, ascl:1208.017
Roger, R. S., & Irwin, J. A. 1982, ApJ, 256, 127
Rumble, D., Hatchell, J., Gutermuth, R. A., et al. 2015, MNRAS, 448, 1551
Rumble, D., Hatchell, J., Pattle, K., et al. 2016, MNRAS, 460, 4150
Sadavoy, S. I., Di Francesco, J., Bontemps, S., et al. 2010, ApJ, 710, 1247
Sadavoy, S. I., Di Francesco, J., Johnstone, D., et al. 2013, ApJ, 767, 126
Salji, C. J., Richer, J. S., Buckle, J. V., et al. 2015a, MNRAS, 449, 1769
Salji, C. J., Richer, J. S., Buckle, J. V., et al. 2015b, MNRAS, 449, 1782
Samson, W. B. 1975, Ap&SS, 34, 377
Savage, B. D., & Mathis, J. S. 1979, ARA&A, 17, 73
Schisano, E., Rygl, K. L. J., Molinari, S., et al. 2014, ApJ, 791, 27
Skinner, S. L., Sokal, K. R., Güdel, M., & Briggs, K. R. 2009, ApJ, 696, 766
Walker, M. F. 1959, ApJ, 130, 57
Ward-Thompson, D., Di Francesco, J., Hatchell, J., et al. 2007, PASP, 119, 855
Ward-Thompson, D., Pattle, K., Kirk, J. M., et al. 2016, MNRAS, arXiv:1608.04353
Watson, M. 2010, Master's thesis, Univ. Hertfordshire
Whitworth, A. P., Bhattal, A. S., Chapman, S. J., Disney, M. J., & Turner, J. A. 1994, A&A, 290, 421
Wilking, B. A., Harvey, P. M., & Joy, M. 1984, AJ, 89, 496
Williams, J. P., de Geus, E. J., & Blitz, L. 1994, ApJ, 428, 693